

Naval Surface Warfare Center
Carderock Division
West Bethesda, MD 20817-5700



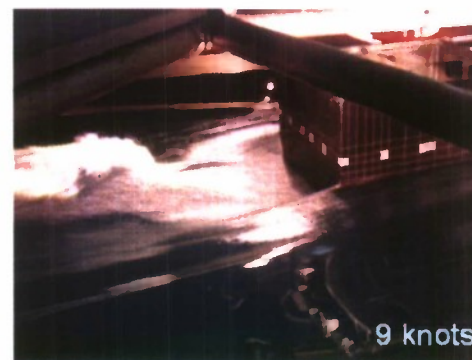
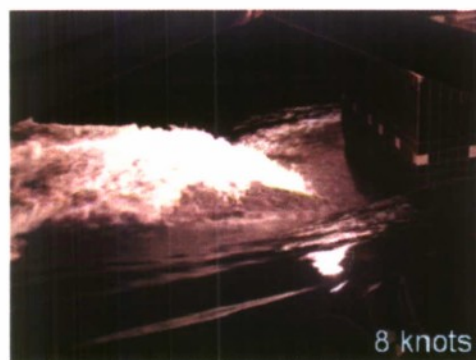
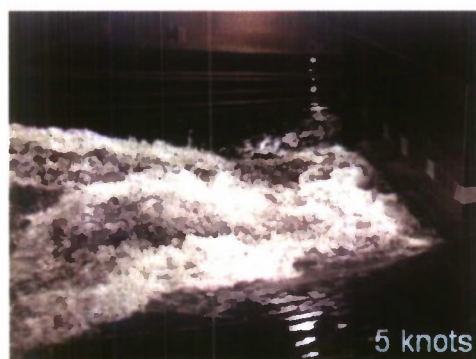
NSWCCD-50-TR-2009/025
Hydromechanics Department Report

May 2009

A Detailed Study of Transom Breaking Waves

By

Thomas C. Fu, Anne M. Fullerton, Toby Ratcliffe, Lisa Minnick, Don Walker,
Mary Lee Pence, and Kirk Anderson



Approved for public release; distribution unlimited.

20090520167

REPORT DOCUMENTATION PAGE			Form Approved OMB No. 0704-0188	
Public reporting burden for this collection of information is estimated to average 1 hour per response, including the time for reviewing instructions, searching existing data sources, gathering and maintaining the data needed, and completing and reviewing this collection of information. Send comments regarding this burden estimate or any other aspect of this collection of information, including suggestions for reducing this burden to Department of Defense, Washington Headquarters Services, Directorate for Information Operations and Reports (0704-0188), 1215 Jefferson Davis Highway, Suite 1204, Arlington, VA 22202-4302. Respondents should be aware that notwithstanding any other provision of law, no person shall be subject to any penalty for failing to comply with a collection of information if it does not display a currently valid OMB control number. PLEASE DO NOT RETURN YOUR FORM TO THE ABOVE ADDRESS.				
1. REPORT DATE (DD-MM-YYYY) May 2009		2. REPORT TYPE Final		3. DATES COVERED (From - To) May 2009
4. TITLE AND SUBTITLE A Detailed Study of Transom Breaking Waves		5a. CONTRACT NUMBER N0001407WX20728		
		5b. GRANT NUMBER		
		5c. PROGRAM ELEMENT NUMBER		
6. AUTHOR(S) Thomas C. Fu, Anne M. Fullerton, Toby Ratcliffe, Lisa Minnick, Don Walker, Mary Lee Pence, and Kirk Anderson		5d. PROJECT NUMBER		
		5e. TASK NUMBER		
		5f. WORK UNIT NUMBER 07-1-5600-159, -171		
7. PERFORMING ORGANIZATION NAME(S) AND ADDRESS(ES) AND ADDRESS(ES) Naval Surface Warfare Center Carderock Division 9500 Macarthur Boulevard West Bethesda, MD 20817-5700		8. PERFORMING ORGANIZATION REPORT NUMBER NSWCCD-50-TR-2009/025		
9. SPONSORING / MONITORING AGENCY NAME(S) AND ADDRESS(ES) Dr. L. Patrick Purtell Office of Naval Research 800 North Quincy Street Arlington, VA 22217-5660		10. SPONSOR/MONITOR'S ACRONYM(S)		
		11. SPONSOR/MONITOR'S REPORT NUMBER(S)		
12. DISTRIBUTION / AVAILABILITY STATEMENT Approved for public release; distribution unlimited.				
13. SUPPLEMENTARY NOTES				
14. ABSTRACT Detailed measurements of the turbulent multiphase flow associated with wave breaking present a unique instrumentation challenge. Measurement systems must be capable of high sampling rates, large dynamic ranges, as well as be capable of making measurements in water, air and optically opaque regions. An experiment was performed in on Carriage 2 in the Deep Water Basin at the Naval Surface Warfare Center, Carderock Division, (NSWCCD) in October 2007 to measure various characteristics of the breaking wave generated from a submerged ship transom. The primary objective of this work was to obtain full-scale qualitative and quantitative flow field data of a large breaking transom wave over a range of conditions, specifically transom drafts and Froude numbers. Several types of measurements were made of the transom stern wave. Sinkage and trim were measured using two string potentiometers. Drag, vertical and side forces were measured using block gages. To quantify the spray and free surface deformation, several techniques were used, including a scanning LiDAR system, laser sheet flow visualization (Quantitative visualization or QViz), and Senix Ultrasonic acoustic distance sensors. Additional measurements were made using the Nortek Acoustic Wave and Current (AWAC) profiler, which measured velocity and acoustic backscatter through <div style="text-align: right;">(continued)</div>				
15. SUBJECT TERMS				
16. SECURITY CLASSIFICATION OF:			17. LIMITATION OF ABSTRACT	18. NO. OF PAGES 48+viii
a. REPORT UNCLASSIFIED	b. ABSTRACT UNCLASSIFIED	c. THIS PAGE UNCLASSIFIED		
				19b. TELEPHONE NUMBER 301-227-7058

14. ABSTRACT (continued)

the water column. An array of impedance void fraction probes was also used to measure the entrained air at various locations and depths behind the stern.

CONTENTS

ABSTRACT.....	1
ACKNOWLEDGEMENTS.....	1
ADMINISTRATIVE INFORMATION	1
INTRODUCTION	2
EXPERIMENTAL APPROACH.....	2
Model Description and Facilities	2
Test Conditions	4
Instrumentation	5
Standard Video and Still Imaging.....	5
Block Gages.....	5
String Potentiometers.....	6
LiDAR.....	6
Senix Ultrasonic Sensors	7
Acoustic Wave and Current Profiler (AWAC).....	8
Defocused Digital Imagery Particle Image Velocimetry (DDPIV).....	9
Void Fraction Probes	10
RESULTS	14
Standard Video and Still Imaging.....	14
Forces.....	14
Trim.....	16
LiDAR.....	17
DLP-Enhanced QViz	21
Wavecuts (Senix Ultrasonic Sensors).....	22
Acoustic Wave and Current Profiler (AWAC).....	23
Defocused Digital Imagery Particle Image Velocimetry (DDPIV).....	27
Void Fraction Probes	28
CONCLUSIONS.....	35
Appendix A: Void Fraction Probe Calibration Procedure and Error Analysis.....	37
References.....	47

FIGURES

Figure 1. Image of the transom model geometry.....	3
Figure 2. Plan and profile views of the transom model geometry.....	3
Figure 3. Image of Model 5673, from above looking forward.	3
Figure 4. Plan view of model mounted under Carriage 2.	4
Figure 5. Wave Boom which holds the ultrasonic sensors.	8
Figure 6. Nortek Acoustic Wave and Current Profiler (AWAC) on bottom mount.....	9
Figure 7. DDPIV camera on lift jack in next to Carriage 2.	10
Figure 8. Plan view schematic of camera position relative to transom model.	10
Figure 9. Cross section of IVFM probe.	11
Figure 10. Void fraction probes on brass strut.....	12
Figure 11. Side view schematic of test set-up (not to scale). The waterline shown represents probe positions relative to calm water conditions at vertical position 1..	12
Figure 12. Still images of transom wake during testing over all tested speeds.	14
Figure 13. Drag force versus model speed for all positions.	15
Figure 14. Vertical force versus speed for all positions.....	16
Figure 15. Average forward and aft trim values over all speeds.	17
Figure 16. Mean wake Profile of model 5673, 5 knots.....	18
Figure 17. Mean wake profile of model 5673, 7 knots.....	18
Figure 18. Mean wake profile of model 5673, 8 knots.....	19
Figure 19. Mean wake profile of model 5673, 9 knots.....	19
Figure 20. 2-D characterization of model 5673 wake, 5 knots.....	20
Figure 21. 2-D characterization of model 5673 wake, 7 knots.....	20
Figure 22. 2-D characterization of model 5673 wake, 8 knots.....	21
Figure 23. 2-D characterization of model 5673 wake, 9 knots.....	21
Figure 24. Example of original and ultrasonic wave record for 9 knot condition. Sonic #1 is closest to centerline of model.....	22
Figure 25. Coefficients of resistance for transom model computed across range of Froude numbers tested.	23
Figure 26. Water level time series	24
Figure 27. AWAC return from centerline for 5, 7, 8, and 9 knots.....	25
Figure 28. AWAC return from 21.75 in (55.2 cm) port of centerline for 5,7,8, and 9 knots.....	26
Figure 29. AWAC return from 51.75 in (131.4 cm) port of centerline for 5,7,8, and 9 knots.....	26
Figure 30. Sample of raw bubble image from DDPIV.	27
Figure 31. Bubble size distribution from DDPIV for 8 and 9 knot cases.....	28
Figure 32. Void fraction distribution from DDPIV for knot case.....	28
Figure 33. Example of data for an underwater probe that sees air bubbles. The red line represents the threshold used in analysis.	29
Figure 34. A close up of data presented in Figure 33. The circles represent the data points collected. The red line represents the threshold used in analysis.	30
Figure 35. Example of data for a probe that is in air and sees water droplets. The red line represents the threshold used in analysis.	30

Figure 36. Example of data for a probe that moves in and out of the free surface. The red line represents the threshold used in analysis.	31
Figure 37. Probe Height vs Void Fraction for 7 knots.....	32
Figure 38. Probe Height vs. Void Fraction for 8 knots.....	32
Figure 39. Void fraction contours at wet transom condition, 7 knots.....	34
Figure 40. Void fraction contours at dry transom condition, 8 knots.....	34

TABLES

Table 1. Test Conditions.....	5
Table 2. Model positions relative to carriage.....	5
Table 3. LiDAR locations and conditions for data collection (locations are relative to the stern of the model).	6
Table 4. Probe heights relative to calm water.....	13
Table 5. Void Fraction Test Matrix	13
Table 6. Trim angle and draft at forward and aft perpendiculars.	17
Table 7. Table of resistance coefficients.....	23

INTERNATIONAL SYSTEM OF UNITS (SI) CONVERSION LIST

U.S. CUSTOMARY	METRIC EQUIVALENT
1 inch (in)	25.4 millimeter (mm), 0.0254 meter (m)
1 foot (ft)	0.3048 meter (m)
1 pound-mass (lbm)	0.4536 kilograms (kg)
1 pound-force (lbf)	4.448 Newtons (N)
1 foot-pound-force (ft-lbf)	1.3558 Newton-meters (N-m)
1 foot per second (ft/s)	0.3048 meter per second (m/s)
1 knot (kt)	1.6878 feet per second (ft/s) 0.5144 meter per second (m/s)
1 horsepower (hp)	0.7457 kilowatts (kW)
1 long ton (LT)	1.016 tonnes 1.016 metric tons 1016 kilograms (kg) 2240 pounds
1 inch water (60F)	248.8 Pascals (Pa)

This page intentionally left blank.

ABSTRACT

Detailed measurements of the turbulent multiphase flow associated with wave breaking present a unique instrumentation challenge. Measurement systems must be capable of high sampling rates, large dynamic ranges, as well as be capable of making measurements in water, air and optically opaque regions. An experiment was performed on Carriage 2 in the Deep Water Basin at the Naval Surface Warfare Center, Carderock Division, (NSWCCD) in October 2007 to measure various characteristics of the breaking wave generated from a submerged ship transom. The primary objective of this work was to obtain full-scale qualitative and quantitative flow field data of a large breaking transom wave over a range of conditions, specifically transom drafts and Froude numbers.

Several types of measurements were made of the transom stern wave. Sinkage and trim were measured using two string potentiometers. Drag, vertical and side forces were measured using block gages. To quantify the spray and free surface deformation, several techniques were used, including a scanning LiDAR system, laser sheet flow visualization (Quantitative visualization or QViz), and Senix Ultrasonic acoustic distance sensors. Additional measurements were made using the Nortek Acoustic Wave and Current (AWAC) profiler, which measured velocity and acoustic backscatter through the water column. An array of impedance void fraction probes was also used to measure the entrained air at various locations and depths behind the stern.

ACKNOWLEDGEMENTS

The authors would like to acknowledge the efforts of James Rice and Lauren Russell (NSWCCD, Code 5600), Eric Terrill and Genevieve Lada (Scripps Institution of Oceanography), Kristine Chevalier, Doug Dommermuth, Trish Sur, and Donald Wyatt (SAIC), and David Jeon, Daegyoun Kim, and Mory Gharib (California Institute of Technology).

ADMINISTRATIVE INFORMATION

The work described in this report was performed by the Maneuvering and Control (Code 5600) division of the Hydromechanics Directorate at the Naval Surface Warfare Center, Carderock Division (NSWCCD). The work was sponsored by the Office of Naval Research under the direction of ONR Program Manager Dr. L. Patrick Purtell (Code 334), performed under contract number N0001407WX20728, and work unit numbers 07-1-5600-159 and 07-1-5600-171.

INTRODUCTION

The physics of the transom stern wave continues to be of great importance to understanding both ship breaking waves and bubble wakes. The full-scale breaking transom stern wave is a complex non-linear turbulent flow field, and while Computational Fluid Dynamics (CFD) codes have demonstrated improved capability in predicting the large-scale Kelvin wave structure for a variety of naval craft, the ability of CFD codes to predict the short-scale surface evolution and the energy dissipation involved in breaking regions, spray sheets, and turbulence has not yet been validated and remains a challenge. The primary objective of this work is to obtain full-scale qualitative and quantitative flow field data of a large breaking transom wave over a range of Froude numbers.

An experiment was performed in the Deep Water Basin at the Naval Surface Warfare Center, Carderock Division, (NSWCCD) in October 2007 to measure various characteristics of the breaking wave generated from a submerged ship transom. Several types of measurements were made of the transom stern wave. Sinkage and trim were measured using two string potentiometers. Drag, vertical and side forces were measured using block gages. To quantify the spray and free surface deformation several techniques were utilized, including a scanning LiDAR system, Digital Light Projection (DLP) enhanced Quantitative Visualization (QViz), and Senix Ultrasonic acoustic distance sensors. Additional measurements were made using the Nortek Acoustic Wave and Current (AWAC) profiler, which measured velocity and acoustic backscatter through the water column. An array of impedance void fraction probes was also used to measure the entrained air at various locations behind the stern and various water depths.

EXPERIMENTAL APPROACH

Model Description and Facilities

This experiment was performed by towing Model 5673 in the Deep Water Towing Basin on Carriage 2. The basin is approximately 22 feet deep, 1886 feet long and 50.96 feet wide, with a maximum carriage speed of 33.8 ft/s (20 knots) (Saunders, 1). The model was towed using a tow post located 270 in (6.9 m) forward of the aft perpendicular. A grasshopper was used 90 in (2.3 m) forward of the aft perpendicular to fix the model in yaw, while still allowing it to pitch.

Model 5673 (shown in Figure 1, Figure 2 and Figure 3) has a transom stern and was designed to minimize the generated bow wave so that the transom wake could be more effectively investigated. The model is about 30 feet (9.1 m) long, with a maximum beam of 5 feet (1.5 m). Figure 4 shows a plan view of the model mounted on Carriage 2.

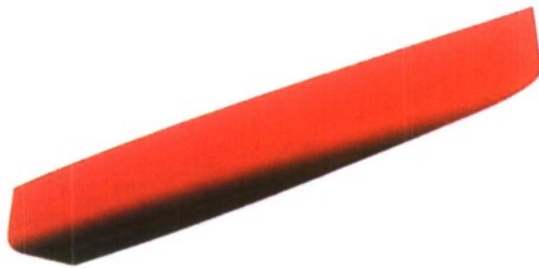


Figure 1. Image of the transom model geometry.

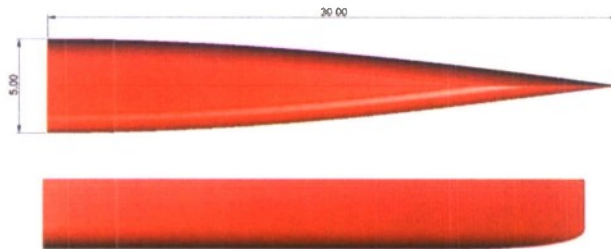


Figure 2. Plan and profile views of the transom model geometry.



Figure 3. Image of Model 5673, from above looking forward.

30-ft Model, facing east

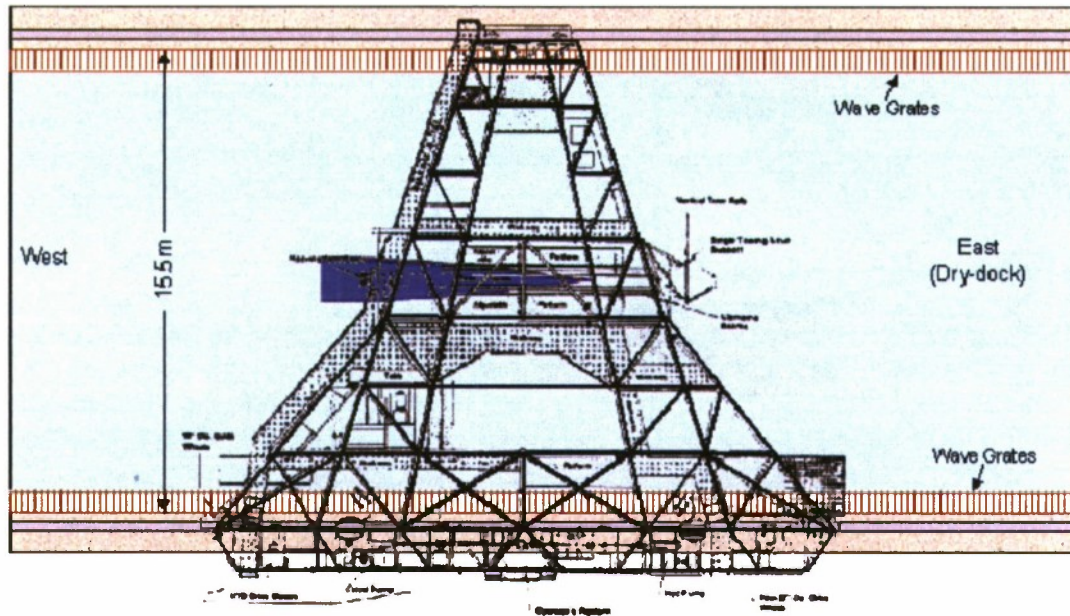


Figure 4. Plan view of model mounted under Carriage 2.

Test Conditions

Though it was intended to test the model at a fixed draft and trim position, the large forces generated prevented this towing configuration. Instead, the model was tested as fixed in heave and free to pitch. The pitch magnitude was recorded during testing. Four different speeds were tested, including 5, 7, 8 and 9 knots. Table 1 shows the test conditions for this experiment, along with the length and draft Froude numbers, where length Froude number is defined as:

$$Fn_L = \frac{v}{\sqrt{gL}} \quad (1)$$

and draft Froude number is defined as:

$$Fn_D = \frac{v}{\sqrt{gD}} \quad (2)$$

where v= model velocity
g=gravitational acceleration
L=length of model (30 ft for this model)
D=drag at the transom

For the 5 and 7 knot conditions the transom was partially wet, and for the 8 and 9 knot conditions the transom was entirely dry. Literature suggests that a transom stern vessel will experience a dry stern (fully ventilated) at draft Froude numbers above 2.5 (Maki et. al., 2, and Faltinsen, 3). In this experiment, the transom stern is dry at a slightly lower draft Froude number of about 2.11.

The model was tested at five different longitudinal positions relative to the carriage to accommodate the various data collection systems that were used. These positions are listed in Table 2.

Table 1. Test Conditions.

Speed (knots)	Length Froude Number (Fn_L)	Draft Froude Number (Fn_D)	Transom Condition
5	0.27	1.4	wet
7	0.38	1.9	wet
8	0.43	2.1	dry
9	0.49	2.3	dry

Table 2. Model positions relative to carriage.

Position	Distance from the east end of the floating girder to the east end of the tow post (along the girder, inches)
1	44.25
2	63.375
3	9.125
4	21.625
5	30.375

Instrumentation

Standard Video and Still Imaging

Four standard frame rate (30 fps) video cameras were used to record video during the test. One camera captured a bow view, and the other three captured images of the free surface aft of the model. Also, a digital still camera was used to record the visual appearance of the free surface aft and around the transom model.

Block Gages

Three calibrated 4 in (10 cm) block gages were used under the tow post to measure the lift, drag and side forces. An additional 4 in (10 cm) block gage was used under the grasshopper to monitor side forces. The block gages were calibrated by NSWCCD, Code 5800, following standard procedures.

String Potentiometers

Model trim was measured using string potentiometers located at the bow and stern of the model. The distance between the string potentiometers was 216.8125 in (5.5 m). The forward string pot was located 288.125 in (7.3 m) forward of the aft perpendicular and the aft string pot was located 71.3125 in (1.8 m) forward of the aft perpendicular. The string potentiometers were calibrated by NSWCCD, Code 5800, following standard procedures.

LiDAR

Light Detection and Ranging, or LiDAR, is a remote sensing system used to collect topographic data. The LiDAR system used during the 2007 Transom Test contains a single Riegl pulsed laser scanner (LMS-Q140-80i) and a four-sided mirror which spun to deflect the laser at different angles along a single line. The time for the reflected pulse to echo back to the sensor receiver is used to calculate distance. The range accuracy of the LMS-Q140-80i unit is generally ± 0.8 in (2 cm), which typically scans in a ± 40 degree sweep at a laser pulse frequency of 30 kHz.

LiDAR data was collected at a rate of 20 Hz. The system was mounted above the transom of the model on a traverse attached to the carriage, in an effort to measure the surface wave field generated in this region. The LiDAR system was mounted 12.7 ft (3.87 m) above the still waterline of the tank and 0.82 ft (0.25 m) starboard of Model 5673. Table 3 shows the locations of the LiDAR for the various data sets that were collected, where the locations are relative to the stern of the model.

Table 3. LiDAR locations and conditions for data collection (locations are relative to the stern of the model).

[illegible]

DLP-Enhanced QViz

A non-intrusive optical technique, Digital Light Projection (DLP) enhanced Quantitative Visualization (QViz), was developed to pursue free surface measurements at high spatial and temporal resolution. A DLP was used to project a laser light sheet perpendicular to the free surface, and video cameras were used to collect digital images of the intersection, representing instantaneous cross-sections of the wave shape. The

latter aspect of the system operation was similar to previous versions of the QViz system, details of which are given in Furey and Fu (4), and Rice et al. (5). However, the introduction of DLP technology permitted several vertical light sheets to be scanned throughout a test run, allowing the free surface to be effectively mapped over a desired area.

The novel projection optics of the DLP-enhanced QViz system used a Digital Micromirror Device (DMD), an optical semiconductor instrument. The DMD device (Texas Instruments, DMD Discovery 1100) contains an array of 1024 by 768 micromirrors. In the system configuration used, it was controlled using a USB interface to project lines onto the free surface that were 1024 mirror pixels long and approximately 10 mirror pixels wide. A timing signal was sent from the DMD device to the video cameras so that the projected images were synchronized with standard, 30 fps, video cameras. The projection optics were mounted on a 2.5 ft by 2.5 ft (0.75 by 0.75 m) square optical breadboard which was required to be located directly above the desired wave region.

Large amounts of free surface image data were collected at five locations. For each location, lines were projected to scan a measurement area of approximately 1.3 by 1.6 ft (0.4 by 0.5 m) within the duration of each run. Approximately 60 cross-sections were obtained for each line. Three locations were centered transversely at 0.66 ft (0.2 m) starboard of the model centerline, and longitudinally at 6.2, 6.9, and 7.9 ft (1.9, 2.1 and 2.4 m) aft of the model transom. Two additional locations were centered longitudinally at 5.9 ft (1.8 m) starboard of the model centerline, 6.6 and 8.2 ft (2.0 and 2.5 m) aft of the model. These two measurement regions represented an effort to collect data across the edge of the breaking region, or shoulder, of the wake.

Senix Ultrasonic Sensors

Seven Senix Ultrasonic sensors, which are non-contact, acoustic instruments for measuring distances through air, were used to collect longitudinal wavecut data. A truss section (wave boom) cantilevered from the basin wall over the water, provided a structure on which the sensors were mounted, as shown in Figure 5. The wave boom extends 22.4 ft (6.83 m) from the basin wall, which places the end of the wave boom approximately 3 ft (0.91 m) short of the basin centerline. A photosensor was set to trigger data collection when the forward perpendicular of the model 24.979 ft (7.61 m) from the sensors. Wave elevation data was collected at a sample rate of 10 Hz. The transverse locations for the sensors, measured outboard from the model centerline, were at y/B (distance outboard divided by the transom beam) of 0.86, 1.13, 1.37, 1.63, 1.88, 2.12, and 2.37. The average height of the sensors off the water level was about 43.5 in (110 cm).

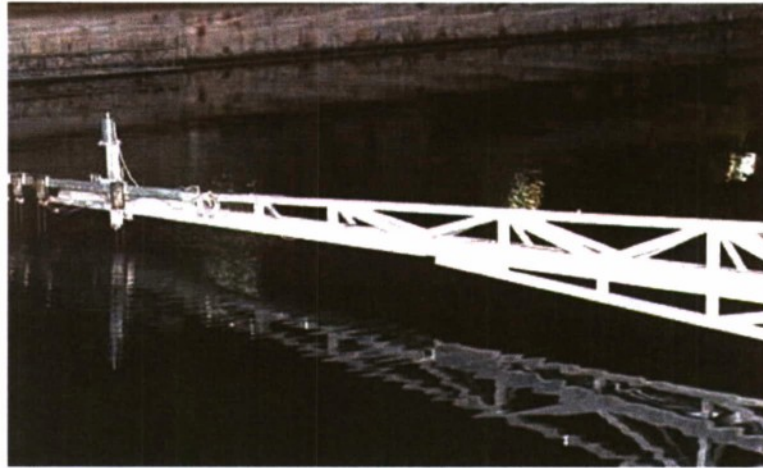


Figure 5. Wave Boom which holds the ultrasonic sensors.

Acoustic Wave and Current Profiler (AWAC)

The Nortek Acoustic Wave and Current Profiler AWAC is an acoustic Doppler current profiler with some added features. In addition to the three acoustic beams angled at 25 degrees from vertical, which are typically found on an ADCP, the AWAC system has a dedicated vertical center beam which is used to measure the water surface through Acoustic Surface Tracking (AST). This center beam transmits a short acoustic pulse that can be finely resolved, allowing for free surface waves of short periods to be accurately measured. The acoustic return at a fine vertical resolution may be correlated to the entrained air in the water. The AWAC is capable of sampling at 4 Hz to capture the surface level; if all bins are recorded to acquire acoustic return through the water column, the sampling frequency is limited to 2 Hz. The AWAC (Figure 6) was stationary during the testing, on a bottom mount about halfway along the length of the tank, located near the wave boom location which held the ultrasonic sensors. Measurements were made over all speeds tested while the AWAC was bottom mounted under the centerline of the model, as well as 21.75 and 51.75 inches port of centerline.



Figure 6. Nortek Acoustic Wave and Current Profiler (AWAC) on bottom mount.

Defocused Digital Imagery Particle Image Velocimetry (DDPIV)

To characterize bubbles, a Defocused Digital Particle Image Velocimetry (DDPIV) camera was employed in an underwater enclosure. DDPIV is a volumetric 3D measurement technique that is capable of measuring large numbers of bubbles at a time. Illumination of the bubbles was provided by a LABest laser that was synchronized with the camera. Images from the camera were recorded to hard drive on computers located on the center aisle.

The DDPIV camera was placed near the centerline of the basin on a lift jack (Figure 7). To measure bubbles, the camera needs the bubbles to be illuminated in forward scatter. To facilitate this, the camera was placed at a 45° angle, facing upward and towards the center aisle (Figure 8). The camera was located 24 in (0.61 m) from the centerline of the model, and 21 in (0.53 m) below the free surface, a depth that was primarily designed to minimize the risk of interference between the model and the camera. The measurement volume was approximately 0.009 in^3 (150 mm^3), and images were collected at 7 double frames per second. The laser was mounted on the center aisle, with optics designed to channel the light underwater. The beam was projected parallel to the free surface at the designed measurement depth.

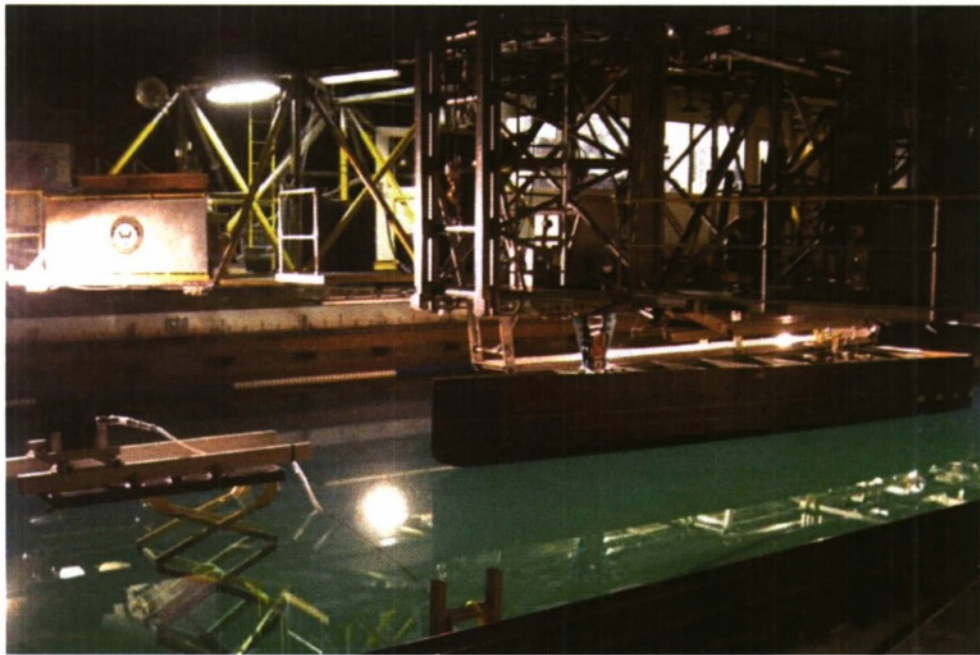


Figure 7. DDPIV camera on lift jack in next to Carriage 2.

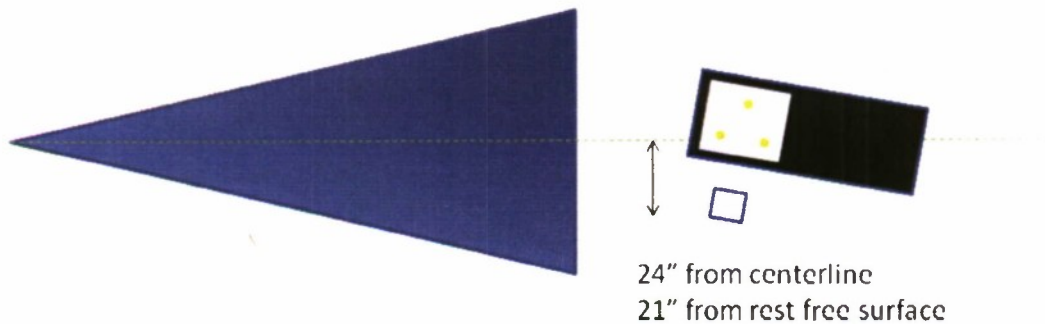


Figure 8. Plan view schematic of camera position relative to transom model.

Void Fraction Probes

A set of six impedance void fraction probes were used to measure the percentage of air in the rooster tail generated by a submerged transom. The design is based on a probe developed by Waniewski (6) to measure void fraction in high-speed, unsteady, multiphase flows. Eight probes were built and used by Coakley et al (7) in the Circulating Water Channel (CWC) at NSWCCD. In this experiment, only six of the Coakley probes were used.

The probes consist of two concentric electrodes separated by insulation as shown in Figure 9. The probe tips are aligned with the tow direction of the model and their small dimensions allow them to respond to individual bubbles. The outer electrode is approximately 0.125 in (0.3 cm) in diameter and is grounded. A sinusoidal voltage signal

of ± 2.5 V and an excitation of 500 kHz are applied to the inner electrode. The impedance across the two electrodes increases with void fraction (% of air) and is mainly resistive for excitation frequencies below the megahertz level. When a bubble comes into contact with the probe, the current between the two electrodes decreases and voltage output of the probe is a large negative spike. The sampling rate of the probes was set at 18 kHz and was determined based on limitations of the data acquisition system.

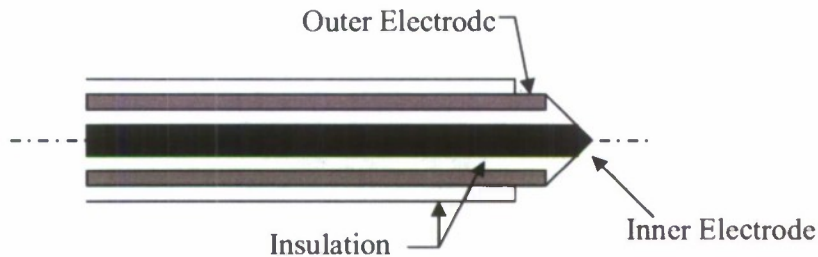


Figure 9. Cross section of IVFM probe.

The probes were mounted on a brass strut and aligned vertically as shown in Figure 10. The probes were positioned on the strut 3.5 in (9 cm) apart, and the strut was attached to an aluminum plate that allowed for vertical movement of the strut. Testing conditions involved two vertical strut positions. Data was collected in vertical position 1 and then the strut was moved 1.75 in (4.5 cm) downward to vertical position 2. This allowed for data to be collected every 1.75 in (4.5 cm) for a vertical span of 19.25 in (49 cm). The strut was attached to a traverse that allowed for the longitudinal position of the probes relative to the transom to be controlled. The traverse provided 3 ft (0.91 m) of longitudinal movement. In addition, the traverse was mounted on slides attached to pieces of aluminum rail which were part of the structure used to mount the void fraction instrumentation to the carriage. The slides were able to move along the rail providing a full testing range of 8 ft (2.4 m), allowing the tip of the probes to be positioned as close as 6 in (15 cm) and as far as 8.5 ft (2.6 m) aft of the transom. The longitudinal locations were chosen so that data was collected throughout the white water region of the wake and to ensure data was collected throughout the rooster tail from its inception to its peak.

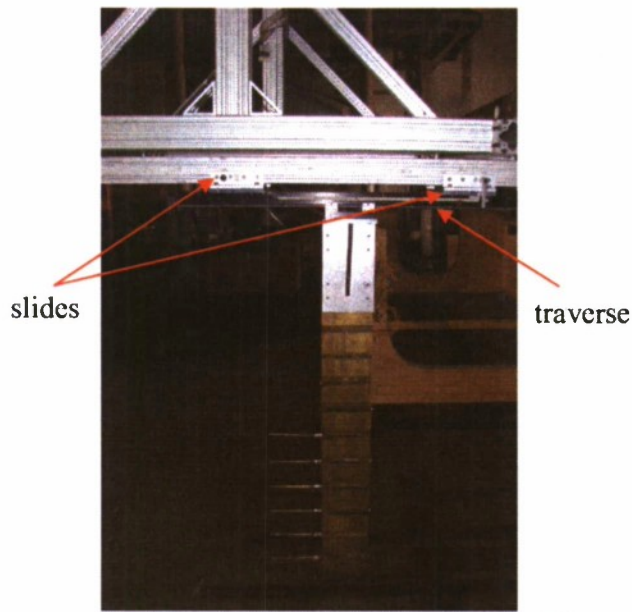


Figure 10. Void fraction probes on brass strut.

Figure 11 shows a schematic of the test set-up. The strut was mounted to the carriage so that the probes were aligned with the tow direction of the model and in line with the model centerline. The probes were held in one position for each run, and moved between runs. Figure 11 shows the calm water waterline relative to vertical position 1. At this position probes 4, 5, and 7 were above the waterline at calm water conditions. There is no probe labeled number 6 because the probe labeling system corresponds to the electronics card associated with the probe and electronics card 6 was not functioning. At vertical position 2 the probe locations are 1.75 in (9 cm) lower than vertical position 1, therefore only probes 5 and 7 were above the calm water waterline. Table 4 provides a summary of probe heights in inches relative to calm water for each vertical position. No data was collected at the probe height of 5.75 in (15 cm) above the calm water level because Probe 5 stopped working while testing before data at vertical position 2 was attained. Void fraction data was collected for one dry transom (7 knots) and one wet transom (8 knots) condition, as shown in Table 5.

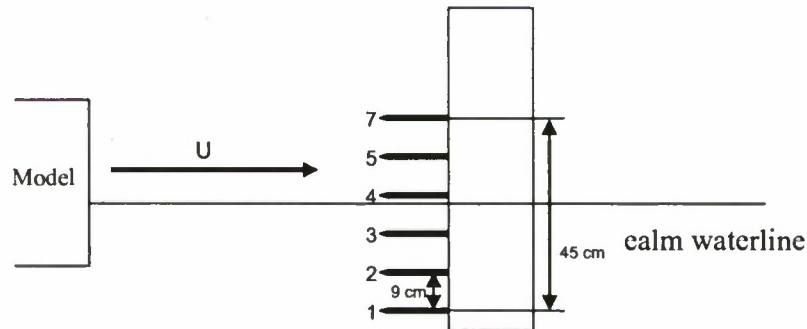


Figure 11. Side view schematic of test set-up (not to scale). The waterline shown represents probe positions relative to calm water conditions at vertical position 1.

Table 4. Probe heights relative to calm water.

Probe #	Height, inches	
	Vert Pos 1	Vert Pos 2
7	7.5	5.75*
5	4	2.25
4	0.5	-1.25
3	-3	-4.75
2	-6.5	-8.25
1	-10	-11.25

*no data was collected at this height

During calibrations, the gain for each probe was set by adjusting the potentiometer in the circuit. The gain is defined as the maximum value the signal reaches when the probe changes mediums. The gain for each probe was set at approximately 2V, except for Probe 2. Probe 2 was extremely sensitive to gain changes meaning that a small adjustment to the potentiometer resulted in a large change in gain. Therefore the smallest gain achievable by Probe 2 was approximately 4V. During testing it was discovered that while the gain had not been physically changed by adjusting the potentiometer, the gains for each probe were different than the initial gains set during calibrations. It is unclear why the gain changed, but it is suspected that it was a result of a flaw in the circuit. No attempt was made to adjust the gains back to calibration, and it was instead decided to perform an extensive post calibration investigation.

Table 5. Void Fraction Test Matrix

Speed knts	Vertical Position	Longitudinal Position inches aft of Transom	# of Runs
7	1	21	2
7	1	26	2
7	1	31	2
7	1	36	2
7	2	21	2
7	2	26	2
7	2	31	2
7	2	36	2
8	1	41	2
8	1	46	2
8	1	51	2
8	1	56	2
8	2	41	2
8	2	46	2
8	2	51	2
8	2	56	2
Total runs =			32

RESULTS

Standard Video and Still Imaging

Figure 12 shows still images recorded of the transom wake during testing over at 5 knots, 7 knots, 8 knots and 9 knots. From these images, it is shown that the 5 and 7 knot conditions are wet transom conditions, while the 8 and 9 knot conditions are dry transom conditions. There was no significant change to the free surface level aft of the transom at 5 knots, though the disturbance corresponding to the depth Froude number change and white water can be seen. The development of the “rooster tail” aft of the stern is apparent at 9 knots.

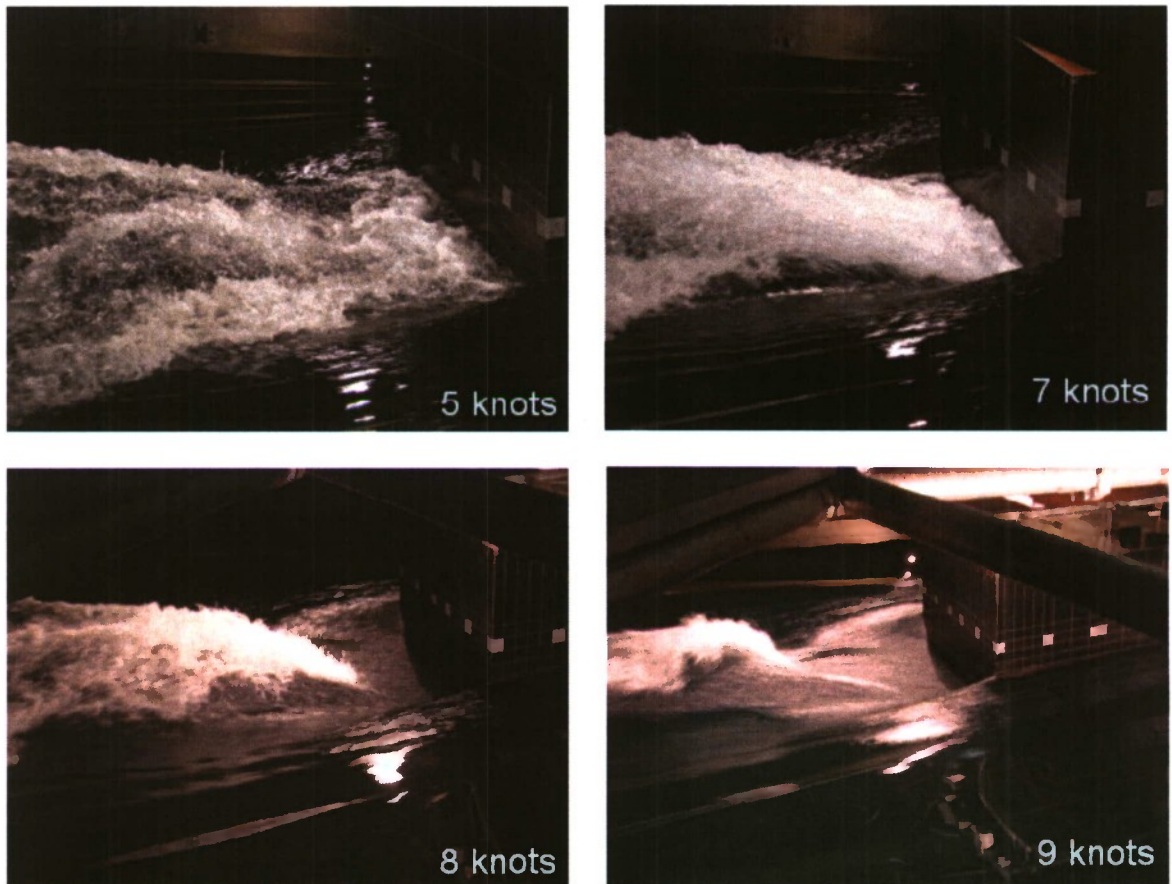


Figure 12. Still images of transom wake during testing over all tested speeds.

Forces

For the following figures, the forces and displacements were averaged over the various longitudinal positions tested (see Table 2 above). Figure 13 shows the average

drag force versus speed for all of the positions over the range of speeds tested. As expected, the magnitude of the drag increases with increased speed. Figure 14 shows the average vertical force versus speed for all of the positions over the range of speeds tested. Vertical force also increases with increased speed. Side force was also monitored during testing to ensure that the model remained aligned properly. Side forces stayed within the allowable range of 1-2% of drag force.

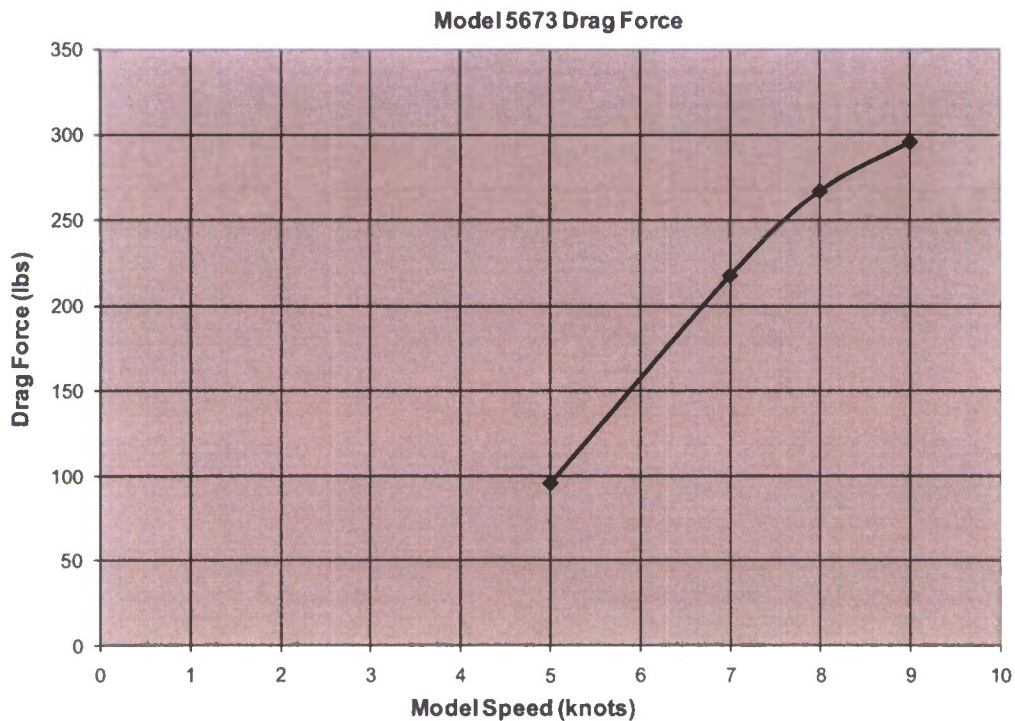


Figure 13. Drag force versus model speed for all positions.

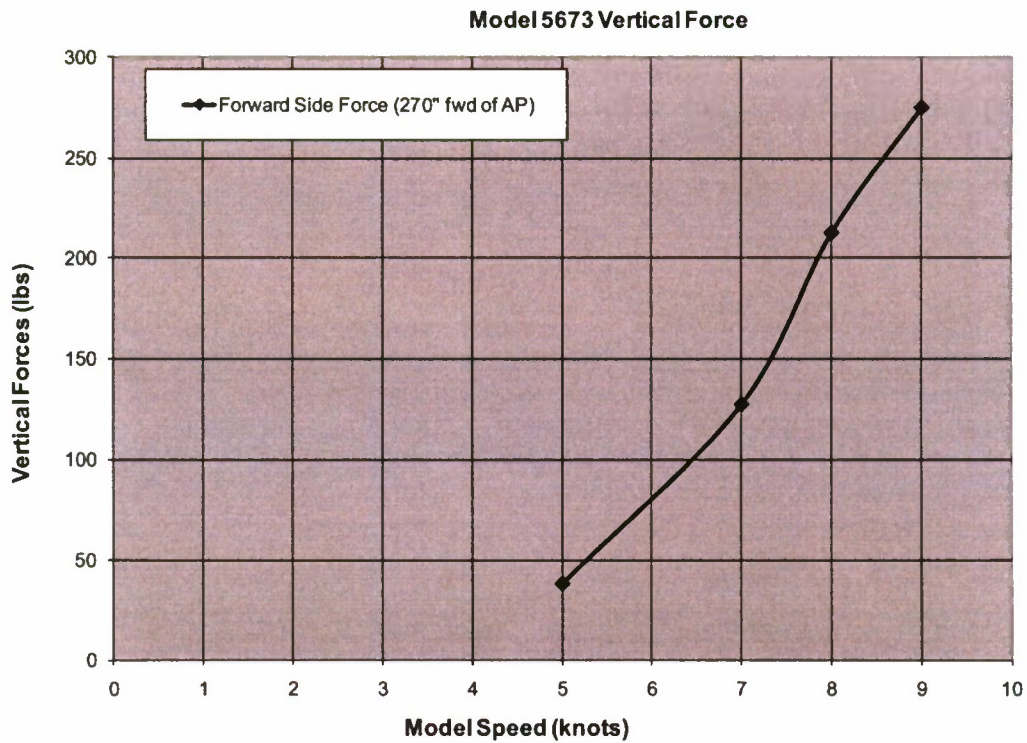


Figure 14. Vertical force versus speed for all positions.

Trim

Figure 15 shows the vertical displacement at the forward and aft string potentiometer versus speed for all positions over the range of speeds tested, where a negative number indicates that the bow has moved up. With the bow moving up and the stern moving down as speed increase, the trim angle is increasing with increased speed. Table 6 shows the calculated trim angle and draft values at the forward and aft perpendicular.

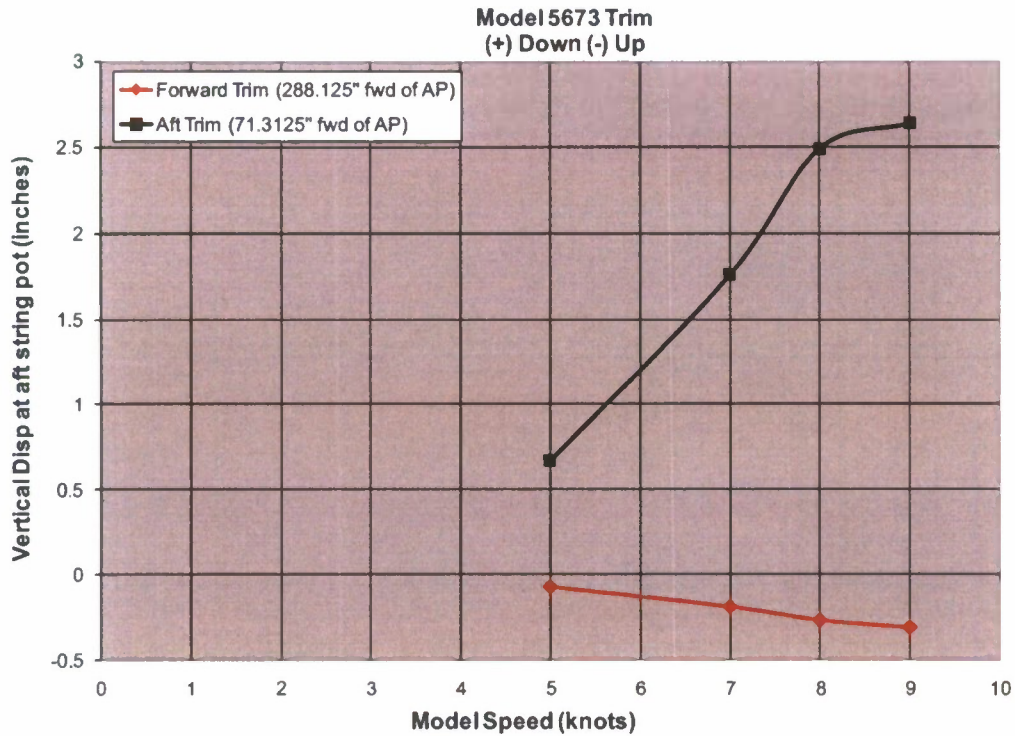


Figure 15. Average forward and aft trim values over all speeds.

Table 6. Trim angle and draft at forward and aft perpendiculars.

Speed	Re_L	Fn_L	Trim Angle	T_{FP}	T_{AP}	Fn_D
(kts)			(deg)	(ft)	(ft)	
5	2.41E+07	0.27	0.19	0.97	1.08	1.4
7	3.37E+07	0.38	0.51	0.93	1.20	1.9
8	3.85E+07	0.43	0.73	0.90	1.29	2.1
9	4.33E+07	0.49	0.78	0.90	1.31	2.3

LiDAR

One transverse wave profile was collected by the LiDAR system during each run. The LiDAR data for the run, was then averaged and corrected for the constant tilt of the system. Mean wake profiles of Model 5673 were then generated. Figure 16, Figure 17, Figure 18, and Figure 19 show the mean wave elevations aft of the model for each of the four speeds 5, 7, 8 and 9 knots, respectively. These plots confirm the expected increase in wave elevation with increase in speed. The data from these runs were also used to create two-dimensional and contour plots in an effort to visually re-create the wake of

Model 5673 and are shown in Figure 20, Figure 21, Figure 22, and Figure 23 for each of the four speeds 5, 7, 8 and 9 knots, respectively. These plots look similar to the still images shown in Figure 12, with very little change in the free surface at the 5 knot condition, and the development of the “rooster tail” at the 9 knot condition.

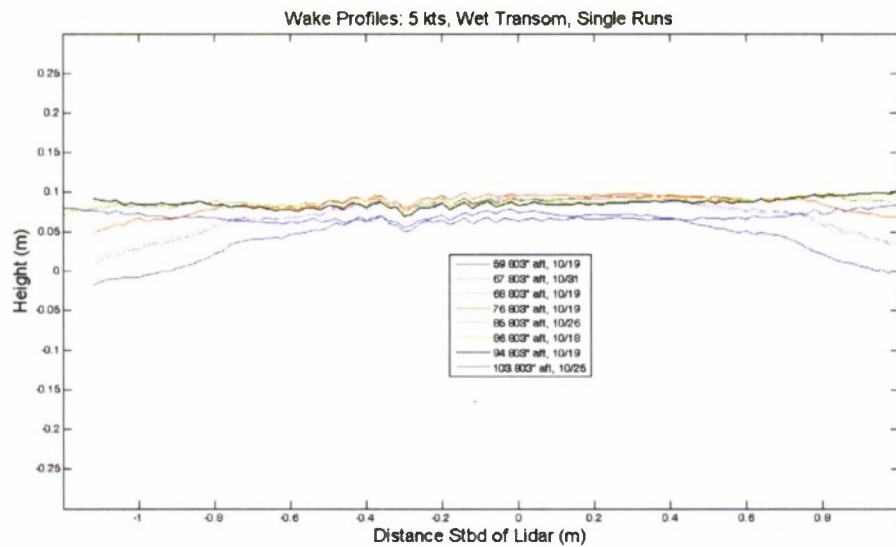


Figure 16. Mean wake Profile of model 5673, 5 knots.

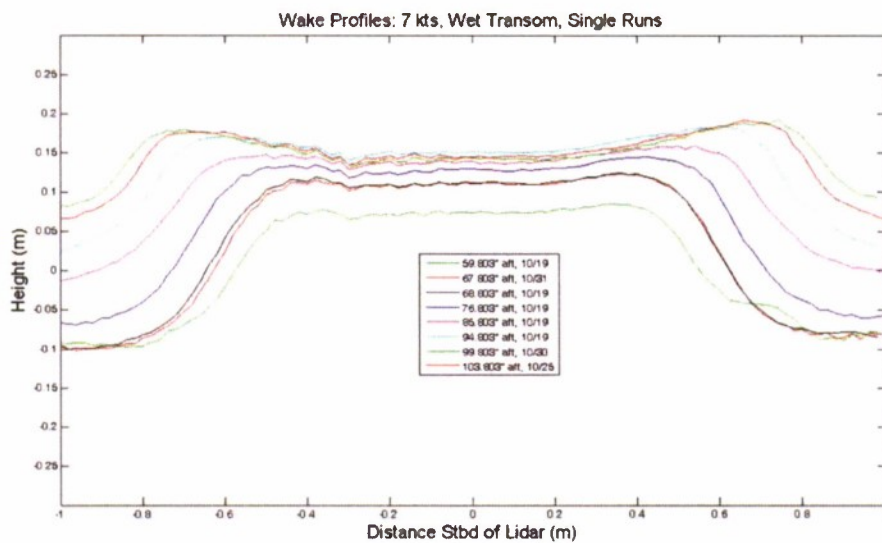


Figure 17. Mean wake profile of model 5673, 7 knots.

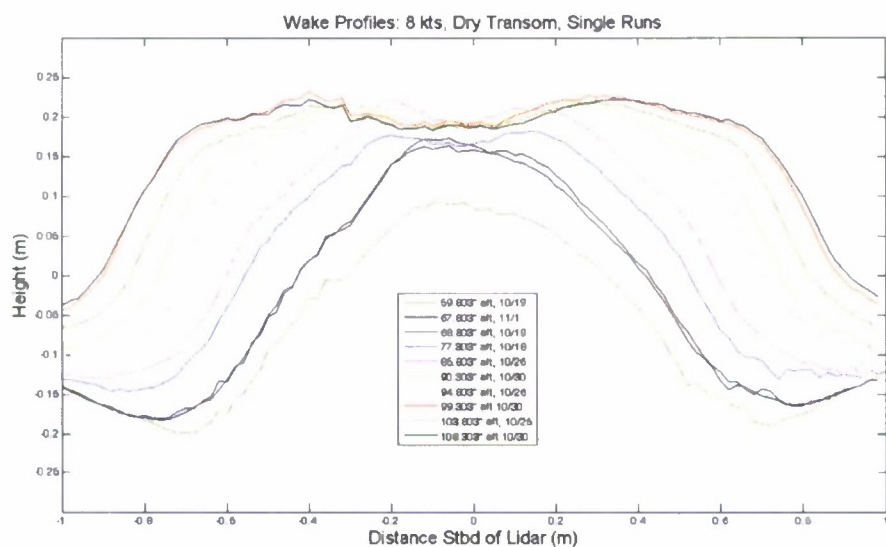


Figure 18. Mean wake profile of model 5673, 8 knots.

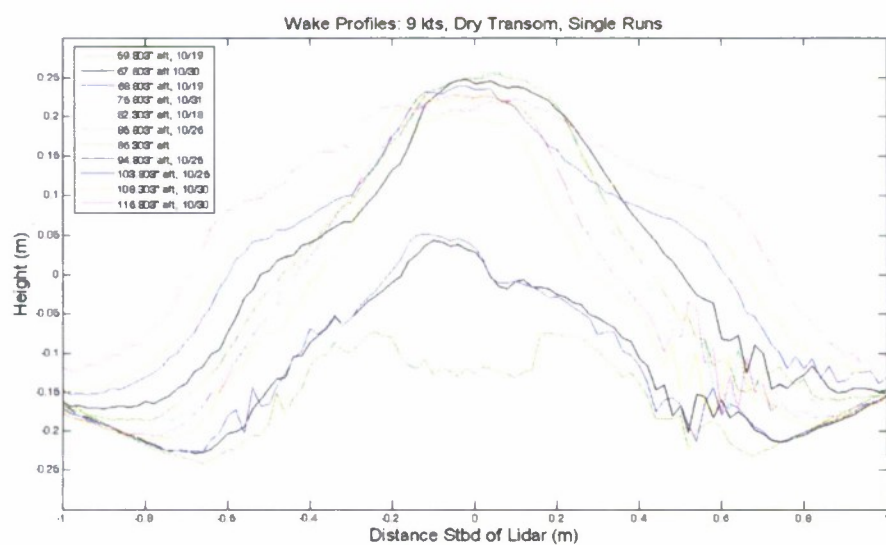


Figure 19. Mean wake profile of model 5673, 9 knots.

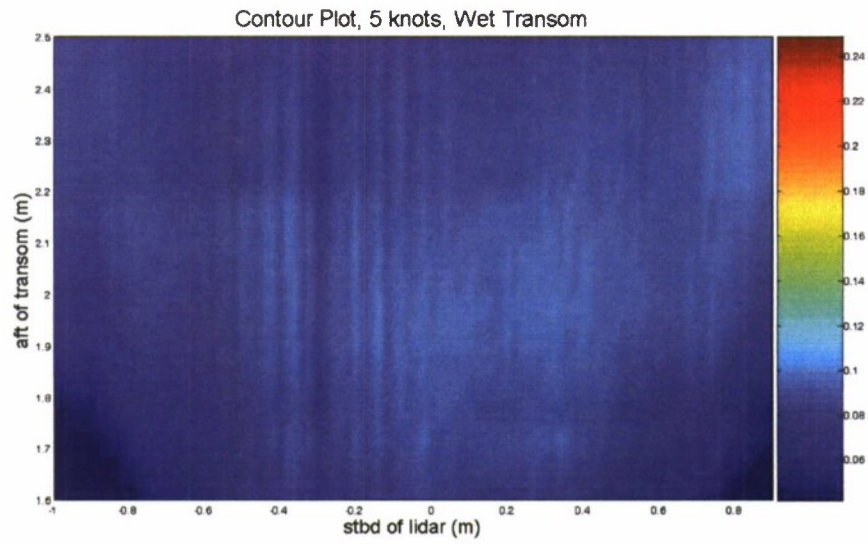


Figure 20. 2-D characterization of model 5673 wake, 5 knots.

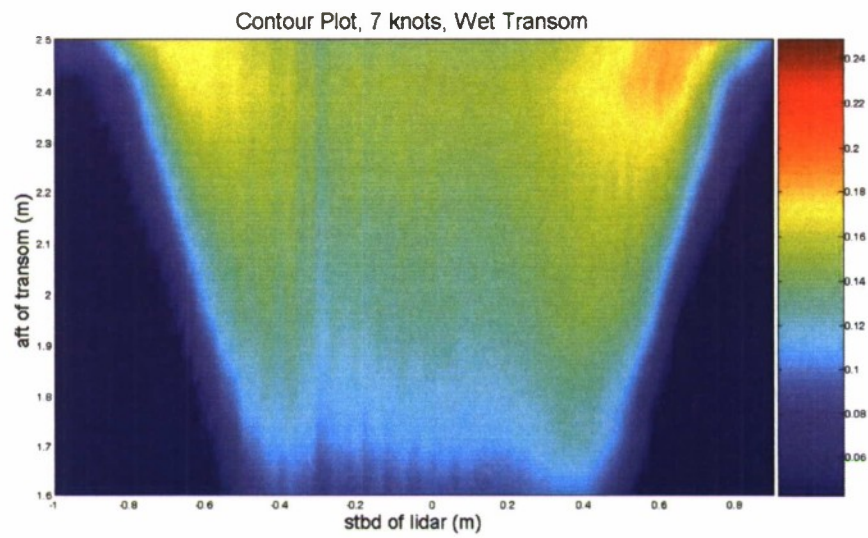


Figure 21. 2-D characterization of model 5673 wake, 7 knots.

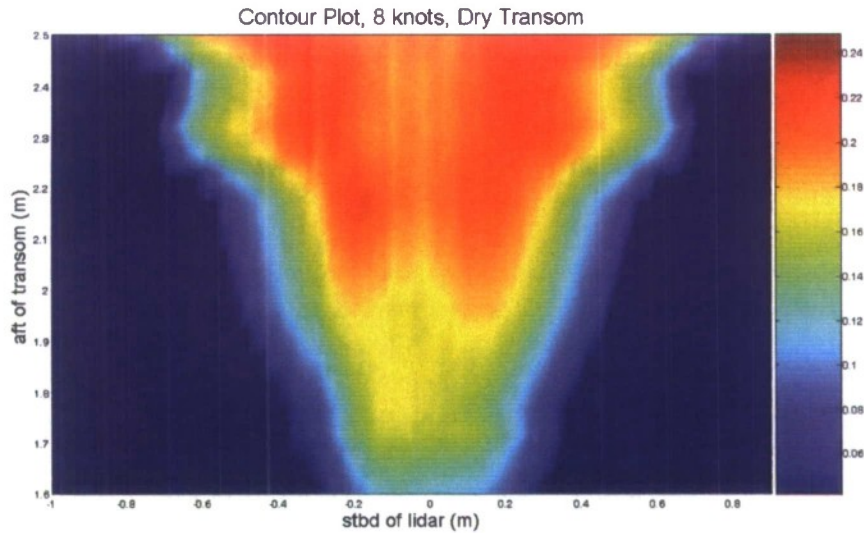


Figure 22: 2-D characterization of model 5673 wake, 8 knots.

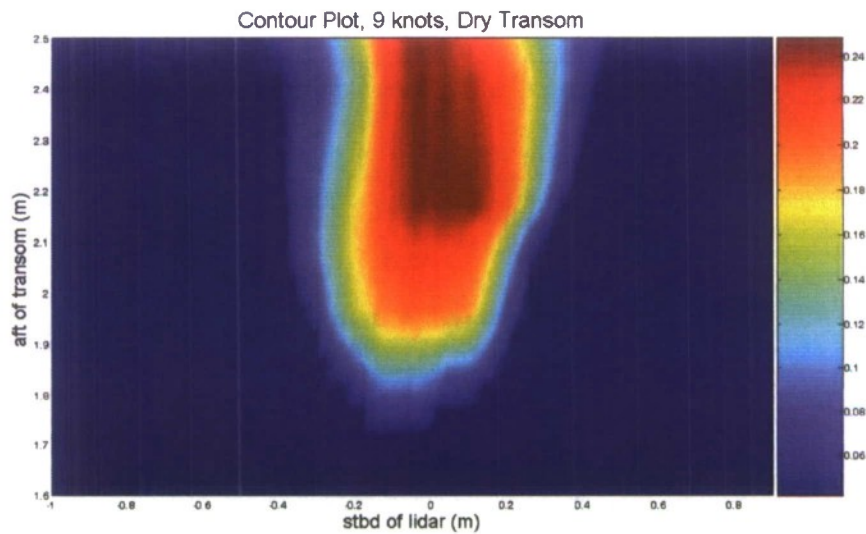


Figure 23: 2-D characterization of model 5673 wake, 9 knots.

DLP-Enhanced QViz

Analysis of the results from the DLP-enhanced QViz system is ongoing. Fluctuations in the free surface profiles, as well as averaged free surface contours, are currently being studied. The ongoing data analysis involves edge detection algorithm development, to identify the free surface in each of the raw images, as well as calibration

method advancement. These results will allow comparisons to be made with other measurements made during testing, as well as with full-scale field measurements of the transom wave of the R/V Athena reported in Fu, et al (8 and 9).

Wavecuts (Senix Ultrasonic Sensors)

The data from the Senix ultrasonic sensors was filtered to remove dropouts and obtain a smooth wave record. Figure 24 shows an example of the data that was collected for the 9 knot condition. The black line represents the original signal, while the red line shows the smoothed, filtered data. This data was then used to calculate the wavemaking resistance coefficient, results of which are tabulated in Table 7 as C_w , along with the other resistance coefficients. These coefficients are plotted in Figure 25. The wave resistance coefficient tends to increase as speed increases for this transom model. Also included in this table are the total resistance coefficients (C_t), the frictional resistance coefficients (C_f), and the residuary resistance coefficients (C_r). The total resistance coefficient is calculated using the measured drag force and the wetted surface area (calculated from the measured sinkage and trim). The frictional resistance coefficient is calculated using the ITTC 57 formula (PNA, 10). Residuary resistance is calculated by subtracting the frictional resistance coefficient from the total resistance coefficient. The wavemaking resistance coefficient makes up part of the residual resistance, along with the eddy resistance. All resistance coefficients are non-dimensionalized by the static wetted surface area at the 1 foot draft, zero trim condition (132.36 ft², 12.3 m²).

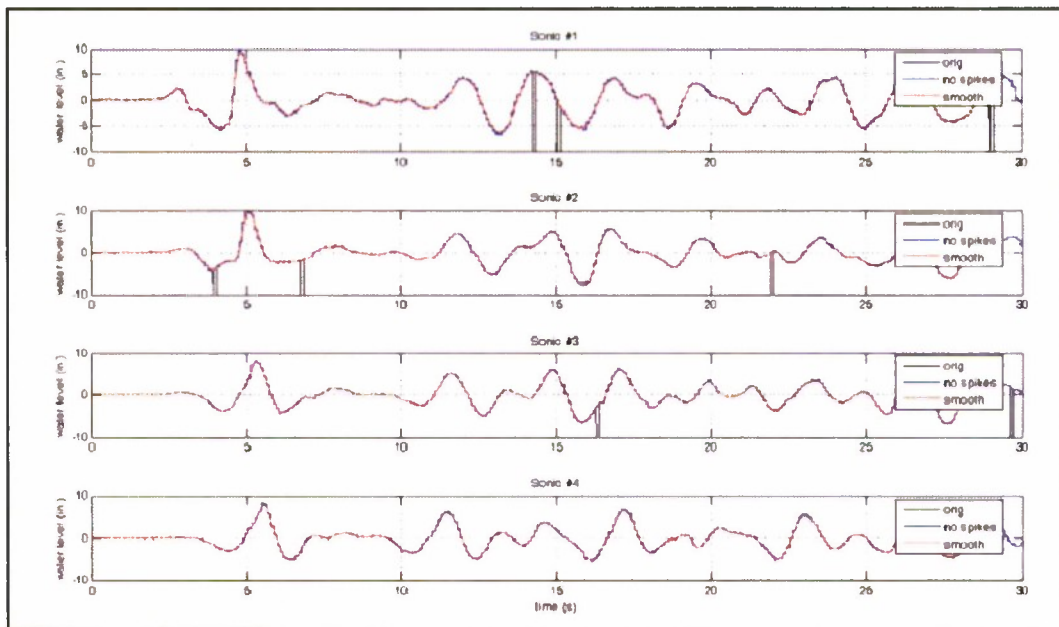


Figure 24. Example of original and ultrasonic wave record for 9 knot condition. Sonic #1 is closest to centerline of model.

Table 7. Table of resistance coefficients.

Speed	Fn_L	R_t	C_t	C_f	C_r	C_w
(kts)	non-dim	(lbs)				
5	0.27	95.9	0.0105	0.0026	0.0079	0.00001
7	0.38	217.3	0.0121	0.0025	0.0097	0.00203
8	0.43	266.9	0.0114	0.0024	0.0090	0.00278
9	0.49	295.5	0.0100	0.0024	0.0076	0.00340

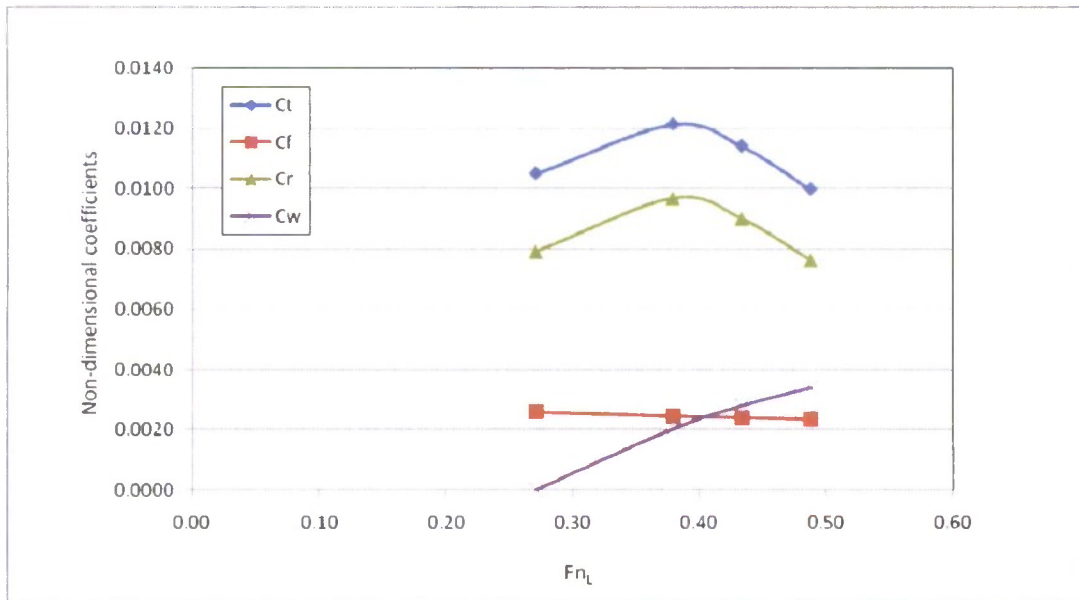


Figure 25. Coefficients of resistance for transom model computed across range of Froude numbers tested.

Acoustic Wave and Current Profiler (AWAC)

Figure 26 shows the water level data collected by the AWAC at the model centerline position, with time converted to distance from the bow. Each panel shows 2 separate runs for each speed, with the 5 knot case in the top panel and the 9 knot case in the bottom panel. The aft edge of the model can be seen in the plot at approximately 30 feet (9.1 m). The wake behind the ship is difficult to resolve from the plots, likely due to the sampling rate of 4 Hz. The transverse wave is apparent in the 7, 8, and 9 knot plots, and the length of this wave increases with vessel speed, as expected.

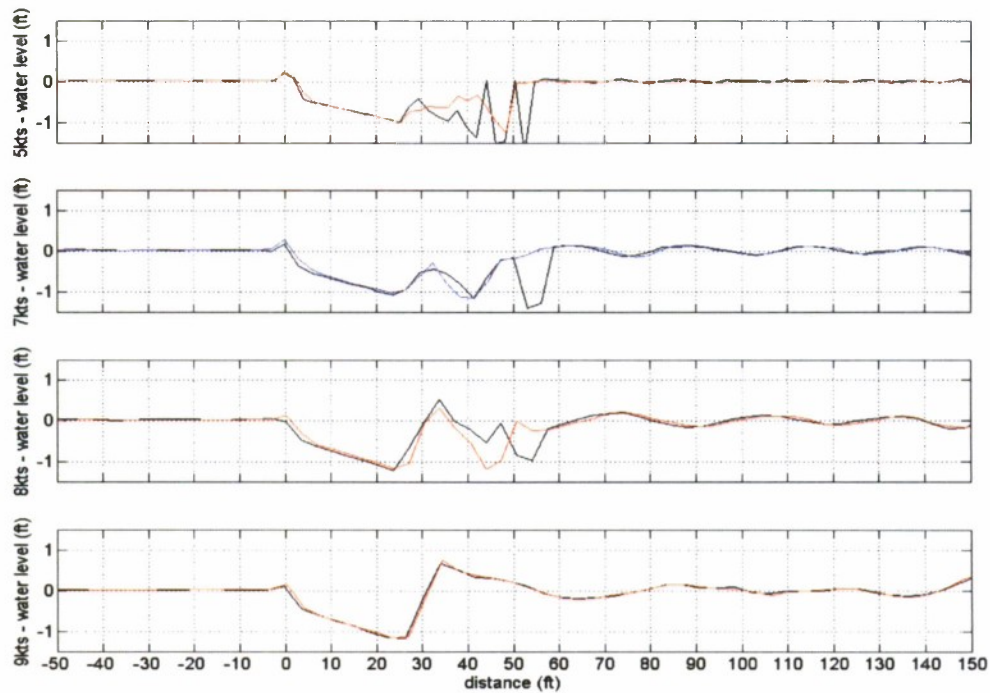


Figure 26. Water level time series

Figure 27 shows the acoustic return for the center beam of the AWAC in counts while the instrument was in the centerline position. Each figure shows a single run, with the time converted to distance past the bow. As with Figure 26, the aft edge of the model can be seen in the plot at approximately 30 feet (9.1 m). Each panel shows a different speed, with 5 knots in the top panel and 9 knots in the bottom panel. The black line shows the level of maximum acoustic return, which is the water surface or the outline of the model. From these plots, it can be seen that the model sinks lower at greater speeds, which was verified through the draft measurements taken during testing. Assuming acoustic return is related to bubble density, it appears that more bubbles are present lower in the water column at lower speeds than at greater speeds.

These plots can be compared with the still images of the flow aft of the transom (Figure 12), which show that at 5 knots, the transom flow is relatively flat with many bubbles behind the hull. From the still photos, it appears that as the speed increases, the density of bubbles observed decreases, resulting in a cleaner flow with bubbles only at the surface, which tends to agree with what is seen in the acoustic return plots. The acoustic plots contain data in raw counts, so further analysis is necessary to facilitate the direct comparison to bubble size and density.

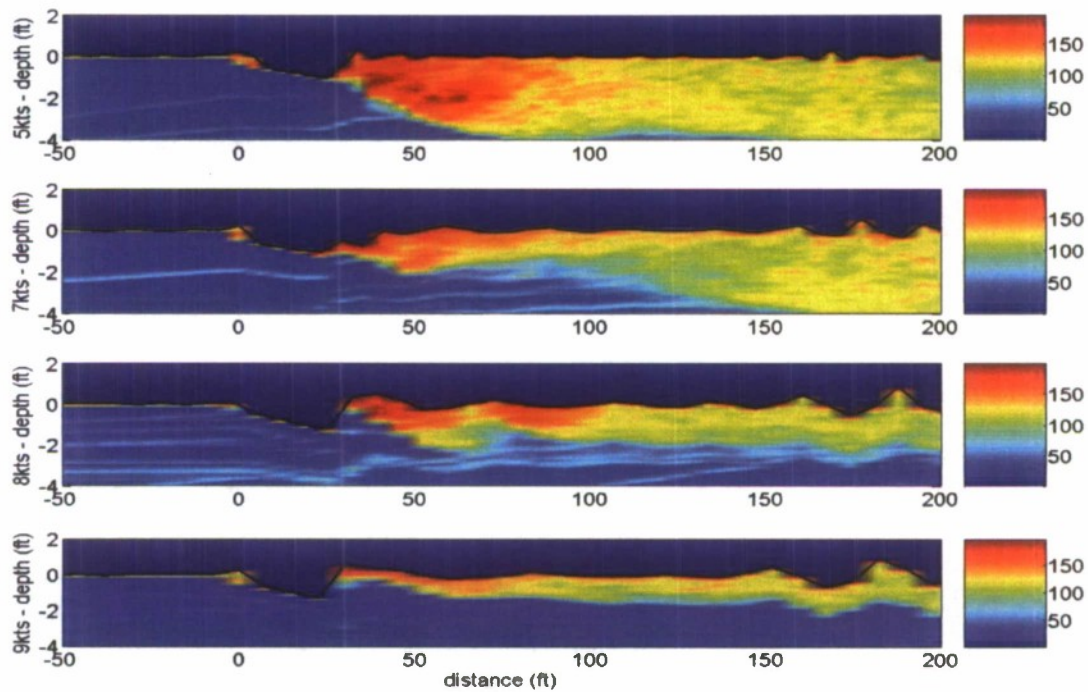


Figure 27. AWAC return from centerline for 5, 7, 8, and 9 knots.

Figure 28 and Figure 29 show the acoustic return for two other locations, 21.75 in (55.2 cm) port of the model centerline and 51.75 in (131.4 cm) port of the model centerline. The AWAC return at the 21.75" port of centerline position looks similar to the return at the centerline position, with a higher intensity return penetrating deeper at the lower speeds than at the greater speeds. The overall acoustic return is much lower at the 51.75 in (131.4 cm) port of centerline position than at the centerline or 21.75 in (55.2 cm) port of centerline position, with very little return other than the water surface, particularly for the higher speeds. This trend makes sense when examining the still photos of the flow (Figure 12), where the bubbles on the surface spread less across the beam of the wake with greater speeds.

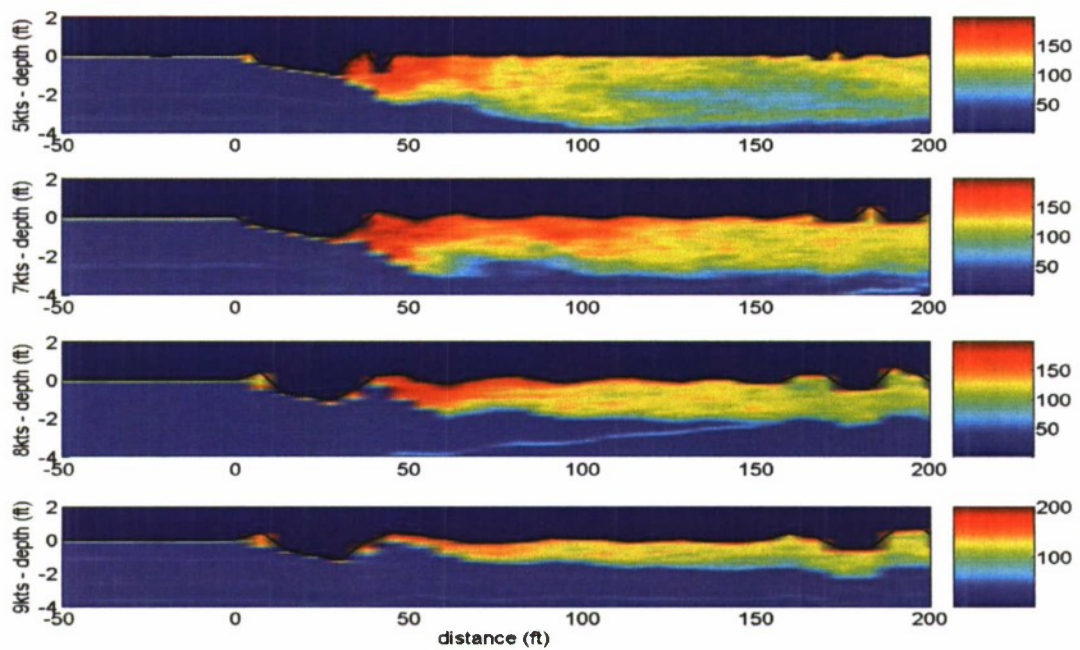


Figure 28. AWAC return from 21.75 in (55.2 cm) port of centerline for 5,7,8, and 9 knots.

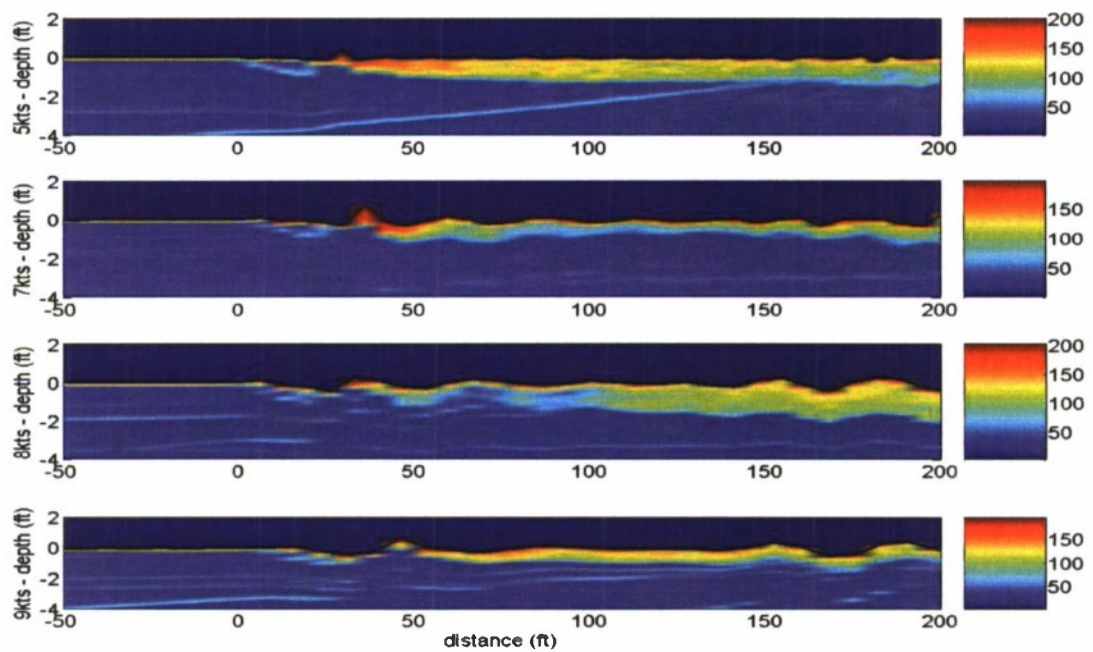


Figure 29. AWAC return from 51.75 in (131.4 cm) port of centerline for 5,7,8, and 9 knots.

Defocused Digital Imagery Particle Image Velocimetry (DDPIV)

Because the camera was fixed to the basin, the DDPIV test procedure was to take images continuously during the carriage transit, and then select the frames which had bubbles present for processing. In most cases, the camera would only capture one frame that had bubbles present for each run. Although the carriage was run at speeds from 7 to 9 knots, bubbles were only present in the imaging volume at the higher speeds (8 and 9 knots). It should be noted that the camera was located 24 in (0.61 m) from the centerline of the model and 21 in (0.53 m) below the surface so as to avoid interference with the model, as indicated in the previous section. The contour plots of the raw signal from the AWAC shown above indicate that there are more bubbles present in this region at lower speeds than higher speeds, which contradicts these results. It may be that though there are fewer bubbles, they are also smaller and more persistent at the higher speeds, allowing the camera to capture these images. The larger bubbles produced at lower speeds will surface more quickly. Also, the AWAC data is in raw form, and needs further processing before it can be used as a proxy for void fraction. Nine cases were recorded at 8 knots and eight cases at 9 knots. A sample of the raw bubble image is shown in Figure 30.



Figure 30. Sample of raw bubble image from DDPIV.

The bubble size distribution is shown in Figure 31. In both the 8 knot and 9 knot cases, the peak of the distribution is around 200 microns. The rise in the distribution at the small diameters is most likely due to spurious data. Although the distribution appears to be slightly shifted towards smaller size at the higher speed, it is unlikely to be a significant difference. The bubble populations were then averaged in columns parallel to the free surface and integrated to obtain void fraction. The void fraction distribution for the 9 knot case is shown in Figure 32. The concentration of high void fraction at depth is most likely indicative of air entrained at the toe of the stern wave which was close to the measurement volume. Corresponding velocity data could confirm this hypothesis.

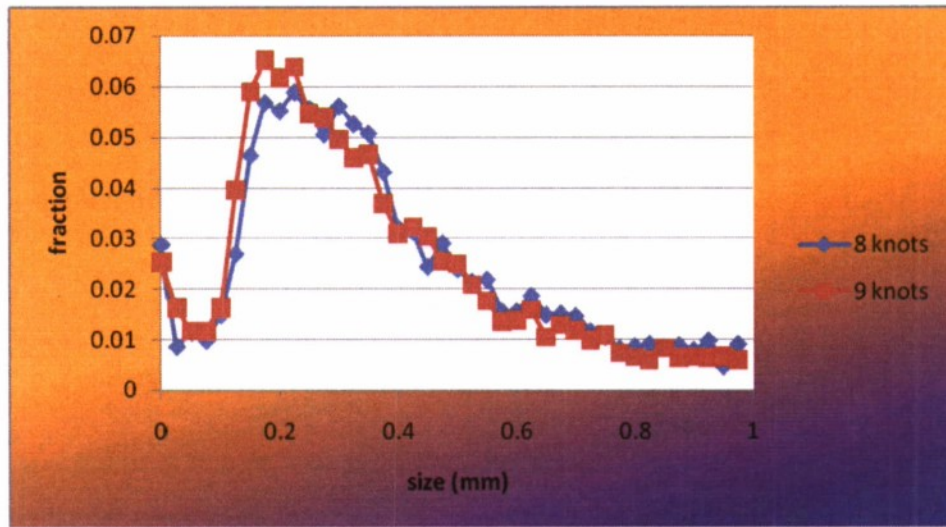


Figure 31. Bubble size distribution from DDPIV for 8 and 9 knot cases.

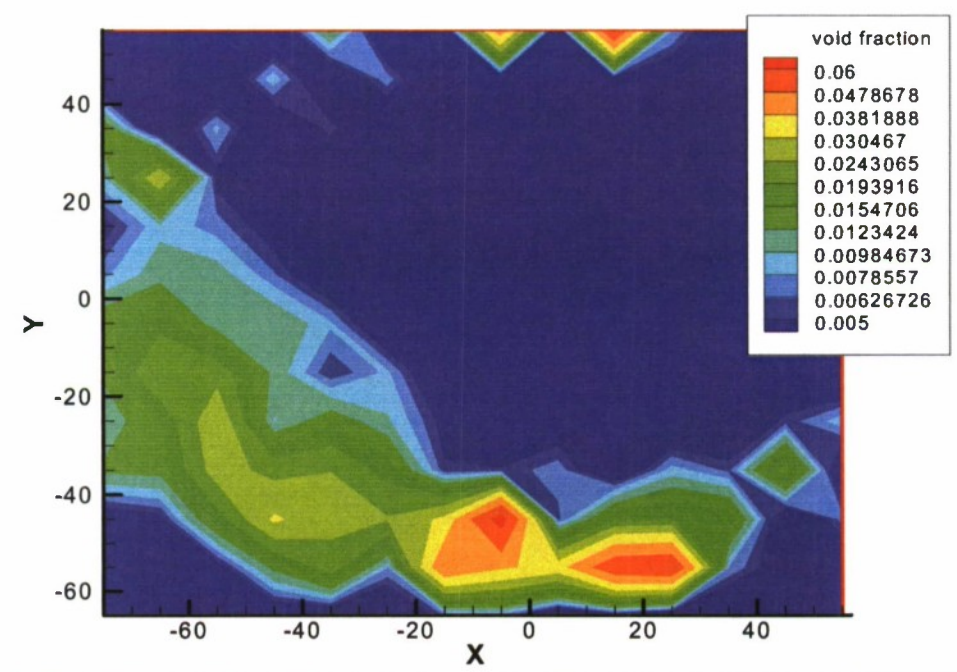


Figure 32. Void fraction distribution from DDPIV for knot case.

Void Fraction Probes

During the experiment probes began a run either in air or water, and depending on the test condition some probes remained out of the water for the entire run. All probes were zeroed in water regardless of whether the probe was submerged or not. For those

probes above the calm water waterline, a cup of water was used to submerge the probe while zeroing, since the baseline condition was considered as submerged.

A voltage signal was observed in the data that would switch between two extremes, which represents a phase change. A probe that was underwater during a run would primarily be at the upper extreme and would spike to the lower extreme when the probe encountered a bubble, as shown in Figure 33 and Figure 34. A probe that was out of the water during a run would primarily be at the lower extreme and would spike to the upper extreme when the probe encounter spray as show in Figure 35. Figure 36 shows data collected for a probe that was near the free surface.

To determine the void fraction level from the data a voltage threshold was applied. All points with a value smaller than the threshold (i.e. lie below the threshold) represent time that the probe is in air. Data points with a value larger than the threshold (i.e. lie above the threshold) represent time the probe is in water. Therefore, the void fraction level, represented by a percentage, was determined by the ratio of the number of data points that are below the threshold (time the probe is in air) to the total number of data points collected. Each probe had its own unique threshold that was determined during calibration. Details of the probe calibration can be found in Appendix A.

Before void fraction levels were calculated the median value of each signal was removed to ensure that all values were properly zeroed before analysis. The probes and electronics were sensitive to changes in the test environment and although zeros were collected before each run occasionally the slightest change in the system would cause the signal to shift. Removing the median ensured the analyzed signal was always zeroed at zero before analysis. In order for the threshold method to be applied to the signal it was imperative that the signal was properly zeroed so that the signal noise fluctuated about zero.

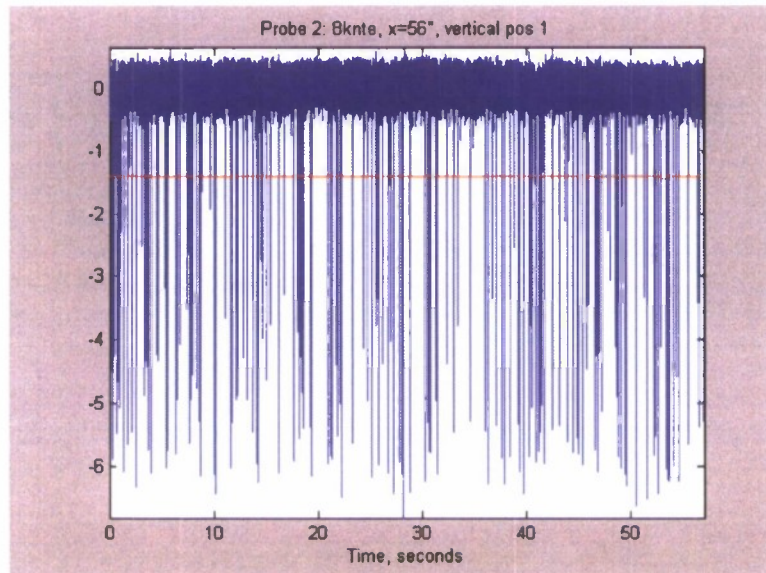


Figure 33. Example of data for an underwater probe that sees air bubbles. The red line represents the threshold used in analysis.

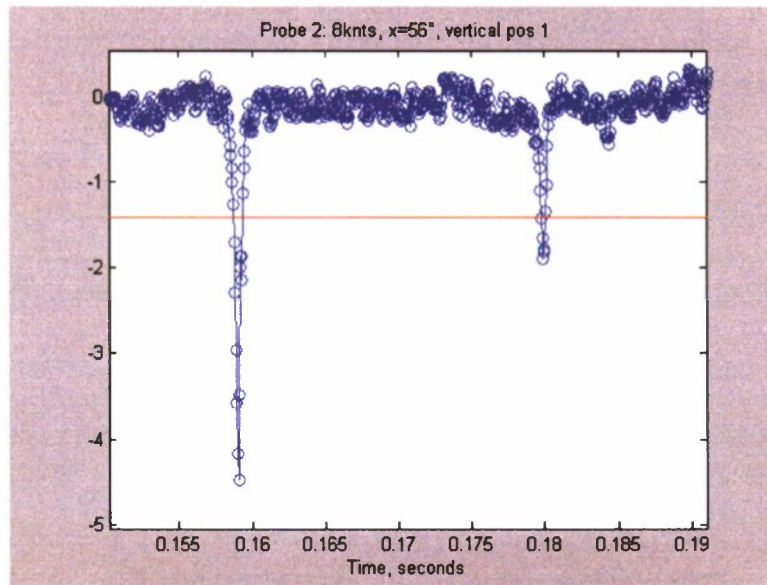


Figure 34. A close up of data presented in Figure 33. The circles represent the data points collected. The red line represents the threshold used in analysis.

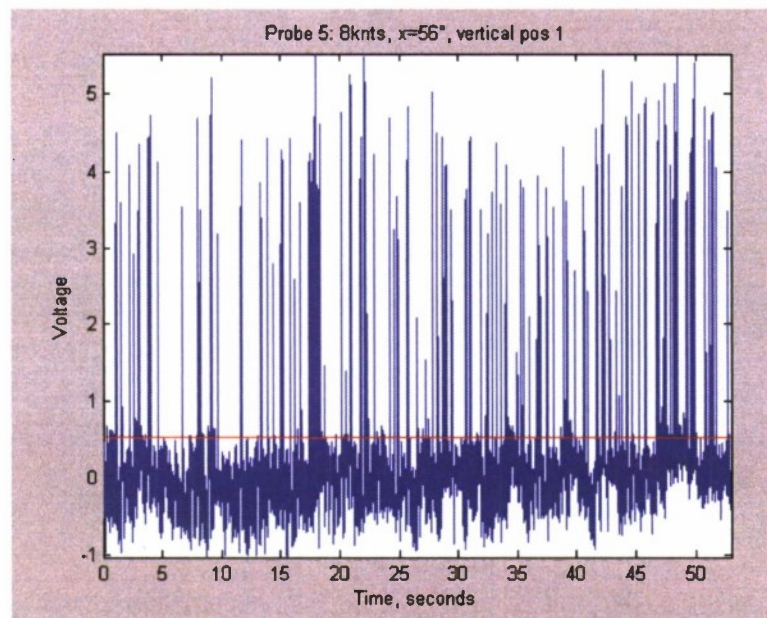


Figure 35. Example of data for a probe that is in air and sees water droplets. The red line represents the threshold used in analysis.

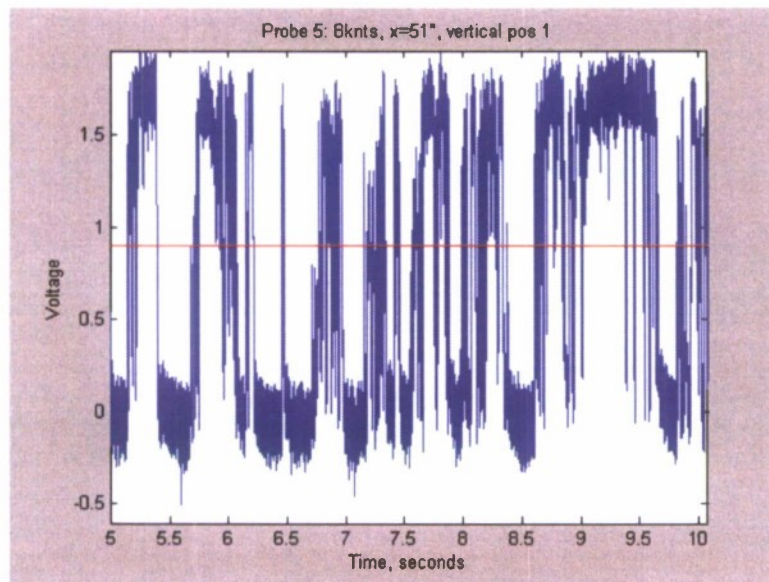


Figure 36. Example of data for a probe that moves in and out of the free surface. The red line represents the threshold used in analysis.

Void fraction data was processed for all runs, and then averaged over the duplicate runs, which is the data presented in this section. Figure 37 and Figure 38 show the variation of void fraction with probe height and longitudinal distance aft of the transom for the two tested speeds of 7 and 8 knots. The probe heights shown in the y-axis are relative to calm water and the legend refers to the distance in inches aft of the transom, with a larger number indicating a greater distance aft of the transom. Error bars are provided for each data point and were calculated using a 95% confidence interval and assuming a t-distribution. Details of this error analysis can be found in Appendix A. The majority of the uncertainty is found in the mid to upper range of void fraction levels, specifically 50-90%. This is expected as both Figure 37 and Figure 38 show that void fraction increases rapidly through this region showing that a small change in probe height results in a large change in percentage of void fraction.

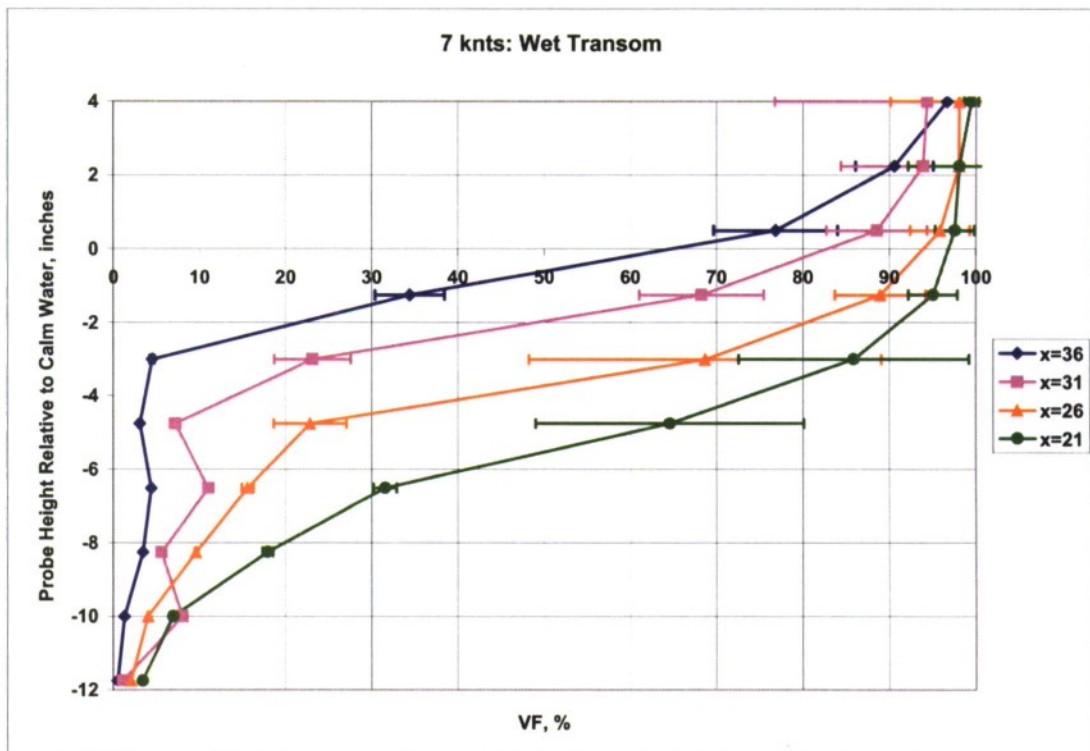


Figure 37. Probe Height vs Void Fraction for 7 knots.

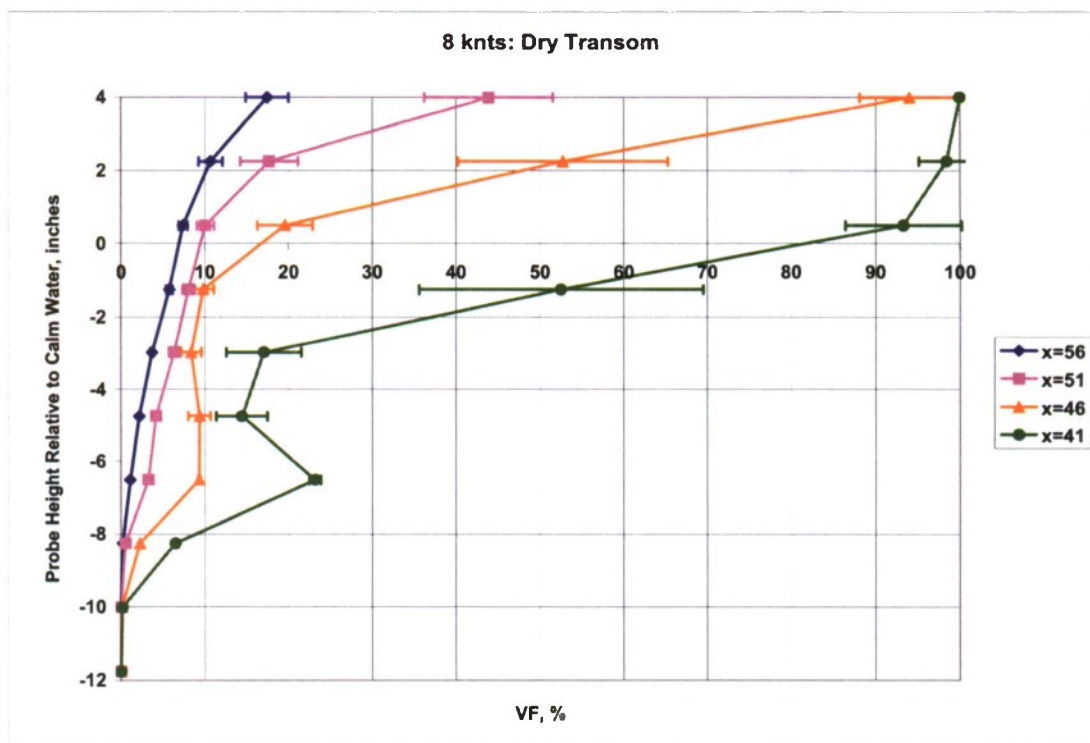


Figure 38. Probe Height vs. Void Fraction for 8 knots.

Figure 39 and Figure 40 show the void fraction contour plots for both the wet and dry transom conditions. The contour lines represent the percent of air in the flow; the 50% contour line is a rough approximation of the free surface. The spacing of the contour lines was chosen based on the error analysis. The spacing is equal to the largest range of error for a given region. For example for void fraction levels ranging from 1-10% the largest error calculated in this range was 2%, therefore, between 1-10% void fraction the contour lines shown are for every 2%. For void fraction levels ranging from 10-30% the spacing is 5% and from 30-100% the spacing is 20%. The x-axis represents the longitudinal distance relative to the transom with negative values indicating a distance aft of the transom. The y-axis provides the probe height relative to calm water. All data was taken along the model centerline and there was no variation in transverse location. The black dots represent the probe locations where data was collected. Longitudinal data was taken every 5 inches and vertical data every 1.75 inches.

The contour plots concur with the visual observations made from the photographs in Figure 12. For the 7 knot, wet transom case, the linear trend of the free surface is confirmed. The plot in Figure 39 shows that the free surface gradually spans a height of approximately 5 inches over a 15 inch longitudinal distance. In contrast, the dry transom case at 8 knots has a steeper climb spanning 5.25 inches vertically over a 9 inch longitudinal distance. The plot in Figure 39 indicates the presence of a small vortex near $x=-31$ " and $y=-10$ " which corresponds to the knob seen in Figure 37 at $x=-31$ " and $y=-10$ ". This vortex is not present at the 8 knot, dry transom condition. While this data shows the presence of a vortex, it is difficult to draw conclusions. It is important to remember the resolution of the grid used in analysis is rough and each condition was only repeated once. This is an area to be explored in more detail in the future.

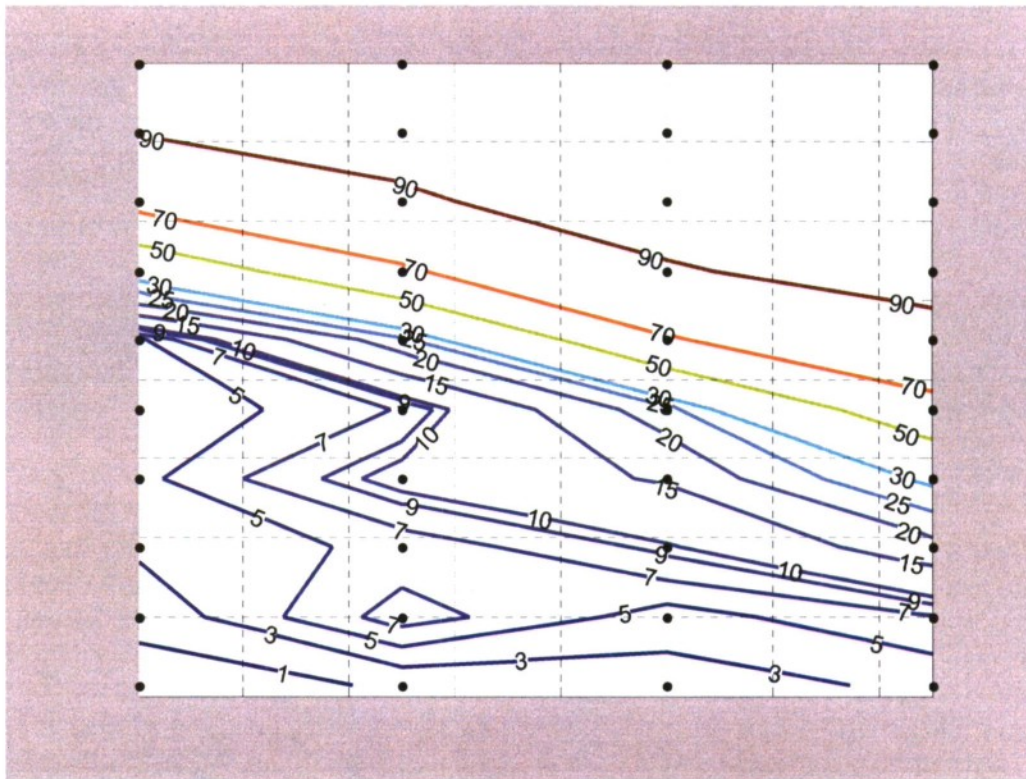


Figure 39. Void fraction contours at wet transom condition, 7 knots.

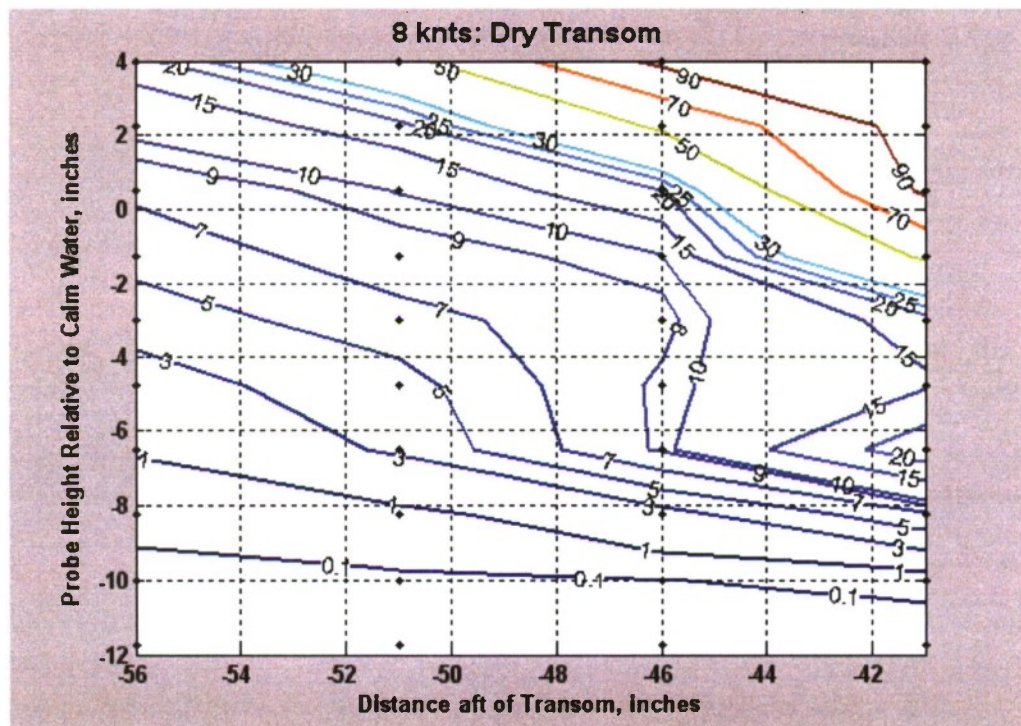


Figure 40. Void fraction contours at dry transom condition, 8 knots.

CONCLUSIONS

A laboratory model capable of producing full-scale transom breaking waves similar in behavior to those of full-scale naval combatants has been designed, fabricated and tested. Multiple measurement methods have been implemented and presented, and comparisons between the still images of the wake and the LiDAR data, AWAC data and void fraction data seem to agree well. The initial experimental work to document and characterize a large breaking transom wave in calm water over a range of transom depth Froude numbers has been completed, and analysis of data continues to provide further comparisons between measurements, as well as insight into the physics of the transom stern wave.

This page intentionally left blank.

APPENDIX A: VOID FRACTION PROBE CALIBRATION PROCEDURE AND ERROR ANALYSIS

Set-Up

The probes were calibrated using the set up shown in Figure A-1. A vertical column was filled with water and had two pressure taps located 12 in (30.5 cm) apart that were each attached to a differential pressure gage. Air stones connected to an air line that was connected to an air compressor were used to inject bubbles into the column of water, creating a two-phase flow. The air stones were placed at the bottom of a half cylinder piece of clear PVC tubing that was mounted flush against one wall of the tank. This allowed the bubbly flow to be confined to the region inside the tube as shown in Figure A-2. The probe was inserted in the top of the half cylinder and aligned with the flow. Due to probe geometry the probe could only be placed a few inches below the uppermost pressure tap. The air compressor was set at a constant pressure and the pressure in the test cylinder was controlled by the valve shown in Figure A-3. Every quarter turn of the valve was marked and data was collected through one full turn of the knob, thus eight valve locations.

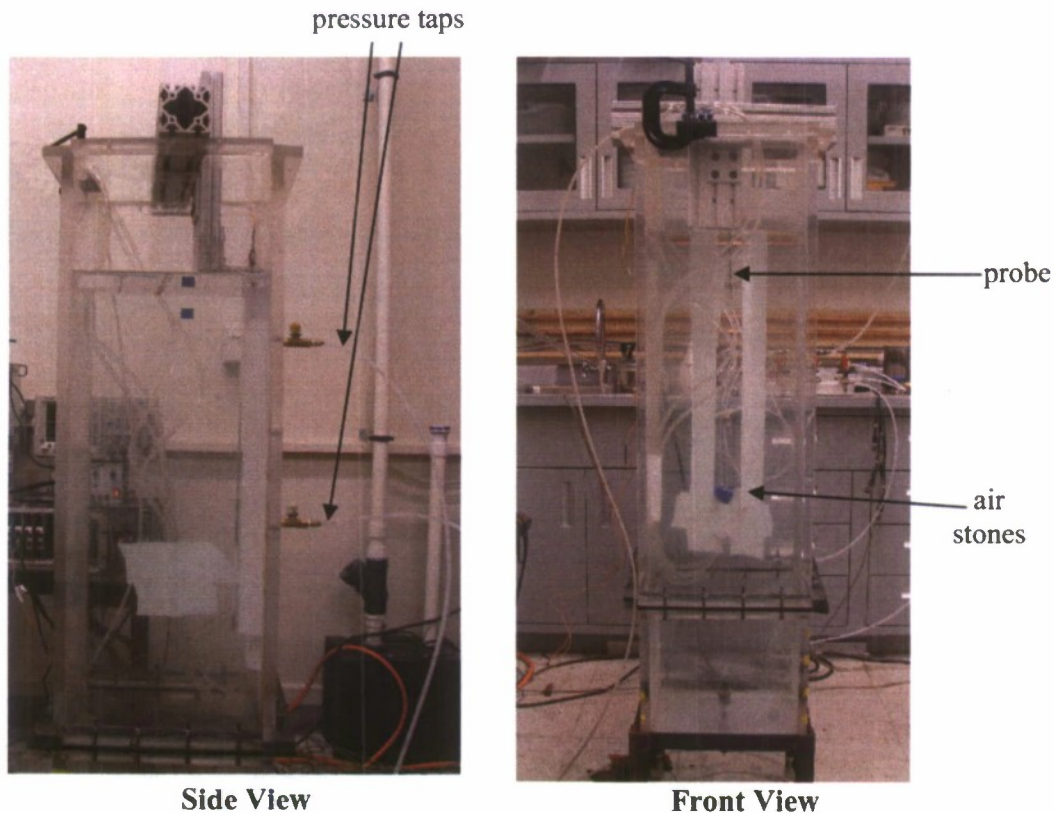


Figure A-1. Water column used to calibrate IVFM.

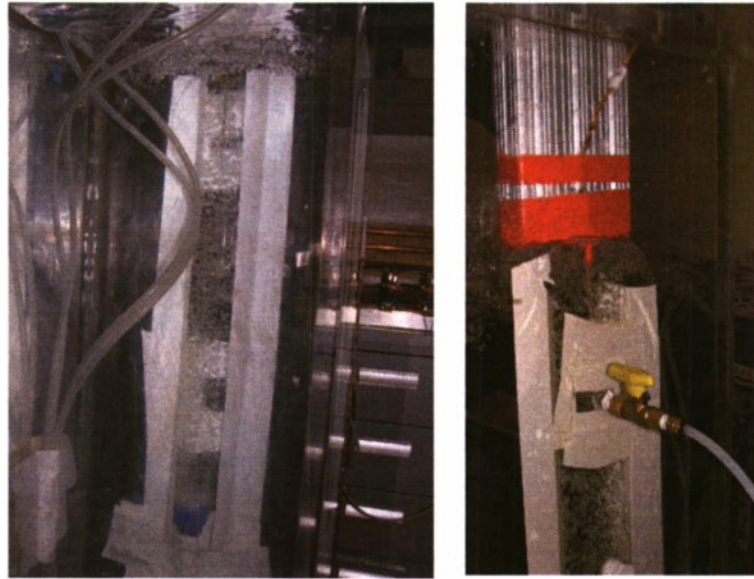


Figure A-2. Pictures showing region of bubbly flow.

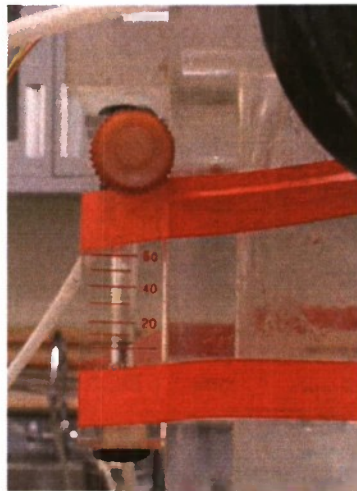


Figure A-3. Regulator valve.

Procedure

The probes were calibrated using a threshold method used by Waniewski (6). Denoting the distance between the pressure taps as H and the differential pressure measured by the pressure gages as h , the steady state void fraction, α , was determined using Equation A-1.

$$\alpha = \frac{h}{H} \quad (\text{A-1})$$

A threshold value was chosen so that the percentage of void fraction data that was below this threshold value was equal to the percentage void fraction (α) calculated with the above equation.

Figure A-4 provides an example of calibration data for one of the void fraction probes. The void fraction measured by the probes using the threshold method is shown in the y axis versus the void fraction calculated using the data collected from the pressure gages. The threshold values were varied to determine which value provided the closest fit to the ideal line represented in the graph by the solid blue line. It was determined for this probe that a threshold of -0.8V was the best match. Each probe was individually calibrated and its corresponding threshold was determined.

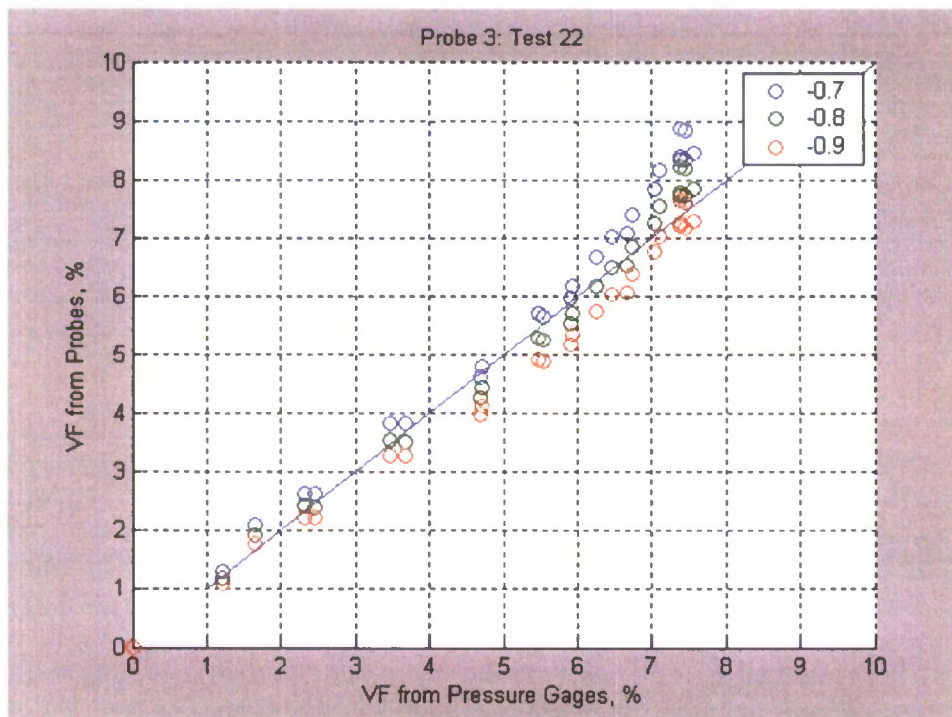


Figure A-4. Example of void fraction probe calibration data.

Error Analysis

Before calibrations the gain for each probe was set by adjusting the potentiometer in the circuit. To set the gain each probe was zeroed while no bubbles were present in the flow. Bubbles were then introduced into the flow so that the probe signal contained the spikes characteristic of the presence of air. The gain was then adjusted so that the spikes peaked at a desired voltage. The largest spike for each probe was set at approximately 2V, except for Probe 2. Probe 2 was very sensitive to gain changes meaning that a small turn of the potentiometer resulted in a large change in gain. Therefore the smallest gain achievable by Probe 2 was approximately 4V.

Once testing began it was discovered that while the gain had not physically been changed by adjusting the potentiometer the gains for each probe were different than the initial gains set during calibrations. Table A-1 summarizes the gains for each probe

during calibrations and testing. It is unclear how the gain changed, but it is suspected that it has to do with an error in the circuit. The circuit appears to be very sensitive to changes in conductivity and resistance and by changing environments from the calibration lab to the carriage the circuit reacted to the new environment and something caused the gains to change. No attempt was made to adjust the gains back to calibration levels while testing for concern that any changes would add further uncertainty. Instead a decision was made to perform an extensive post calibration investigation.

Table A-1. Summary of gains during calibrations and testing.

Probe	Initial Calibration	Testing	Post Cal 1	Post Cal 2
	Gain (V)	Gain (V)	Gain (V)	Gain (V)
1	2.0	1.5	1.8	2.0
2	4.3	6.0	4.0*	4.3
3	1.95	1.2	1.35	2.0
4	2.15	1.4	1.65	2.15
5	2.05	5.0	**	**
7	2.15	1.8	1.9	2.0
* Probe 2 had a gain higher than the limit (10V), it was manually set to 4V before data for Post Calibration 1 was collected				
**Probe 5 was damaged during testing and has not been repaired.				

After testing was completed the instrumentation was returned to the calibration lab and set up to repeat the initial calibrations performed before the test. Post Calibration 1 was performed “as is” with no adjustments made to the gain allowing the instrumentation to be as close to carriage conditions as possible, however Table A-1 shows that the gains were still different than testing conditions. The gain for Probe 2 was so large that it surpassed the limit of the electronics and the signal was clipped. Therefore, a post cal could not be performed on the probe as is. Instead the gain was set to 4V for Post Calibration 1. Post Calibration 2 was performed by adjusting the gain as best as possible back to the values present in the initial calibration. For each set of gains tested a corresponding set of threshold values were determined. These values are summarized in Table A-2. The results of the post calibrations show that threshold varies with gain. However, the lack of a clear trend between the two indicates that threshold is not solely dependent on gain and there are other factors that may affect the threshold values chosen.

Table A-2. Summary of calibrations, gains, and threshold values.

Probe	Calibration	Gain, V	Threshold, V
1	Initial	2	0.6
	Post 1	1.8	0.55
	Post 2	2	0.55
2	Initial	4.3	1.5
	Post 1	4	1.3
	Post 2	4.3	1.2
3	Initial	1.95	0.8
	Post 1	1.35	0.4
	Post 2	2	0.4
4	Initial	2.15	0.8
	Post 1	1.65	0.45
	Post 2	2.15	0.55
7	Initial	2	0.9
	Post 1	1	0.4
	Post 2	2	0.5

The test data was processed using the three different sets of threshold values determined from the initial and post calibrations. The void fraction levels at each longitudinal location and probe heights were compared and are shown in Figures A-5 through A-12. For both speeds at all longitudinal locations, the trend of the data is consistent regardless of which set of threshold values are used. The variation in threshold values simply shifts the data. There is less variation among the different threshold values for the wet transom case at 7 knots than there is at the dry transom case at 8 knots. Since the trend of the data was the same regardless of threshold, the average void fraction profile at each longitudinal location was calculated and that is the data presented in this report.

The random uncertainty, P , was calculated at each probe location for all longitudinal locations using equation A-2.

$$P_i = tS_i \quad (\text{A-2})$$

The value for t is determined assuming a 95% confidence interval and $N-1$ degrees of freedom. N represents the sample size and in this case $N=3$ since there are 3 different threshold values for each probe that were used to process the data. S_i is the sample standard deviation and is determined by equation A-3.

$$S_x = \left[\frac{1}{N-1} \sum_{i=1}^N (X_i - \bar{X})^2 \right]^{\frac{1}{2}} \quad (\text{A-3})$$

The random uncertainty was calculated for both speeds at each longitudinal location and probe height and is summarized in Table A-3. These values were used for the error bars shown in Figure 37 and Figure 38.

Table A-3. Summary of Random Uncertainty (P) values.

Probe	Probe Height relative calm water, in	8 knots				7 knots			
		x=56	x=51	x=46	x=41	x=36	x=31	x=26	x=21
1	-11.75	0.0000	0.0000	0.0000	0.0000	0.0005	0.0060	0.0165	0.0312
	-10	0.0000	0.0000	0.0000	0.0000	0.0063	0.3063	0.0452	0.0612
2	-8.25	0.0001	0.0005	0.0052	0.0414	0.0244	0.0746	0.1774	0.5995
	-6.5	0.0021	0.0189	0.1402	0.6939	0.0605	0.5621	0.6831	1.3411
3	-4.75	0.0753	0.2983	1.3189	3.0530	0.1319	0.6034	4.2405	15.5476
	-3	0.2193	0.6255	1.1848	4.4714	0.2649	4.4489	20.4126	13.3245
4	-1.25	0.3916	0.7534	1.2708	16.9517	4.0106	7.2085	5.2721	2.8431
	0.5	0.5269	1.0242	3.2996	6.9186	7.1747	5.8156	3.4388	2.2625
7	2.25	1.4404	3.4408	12.5197	3.2675	4.4715	9.4828	4.7959	5.8989
	4	2.5598	7.6642	5.8957	0.1123	1.9652	17.5811	7.9311	0.8602

Calibration Comparison Plots

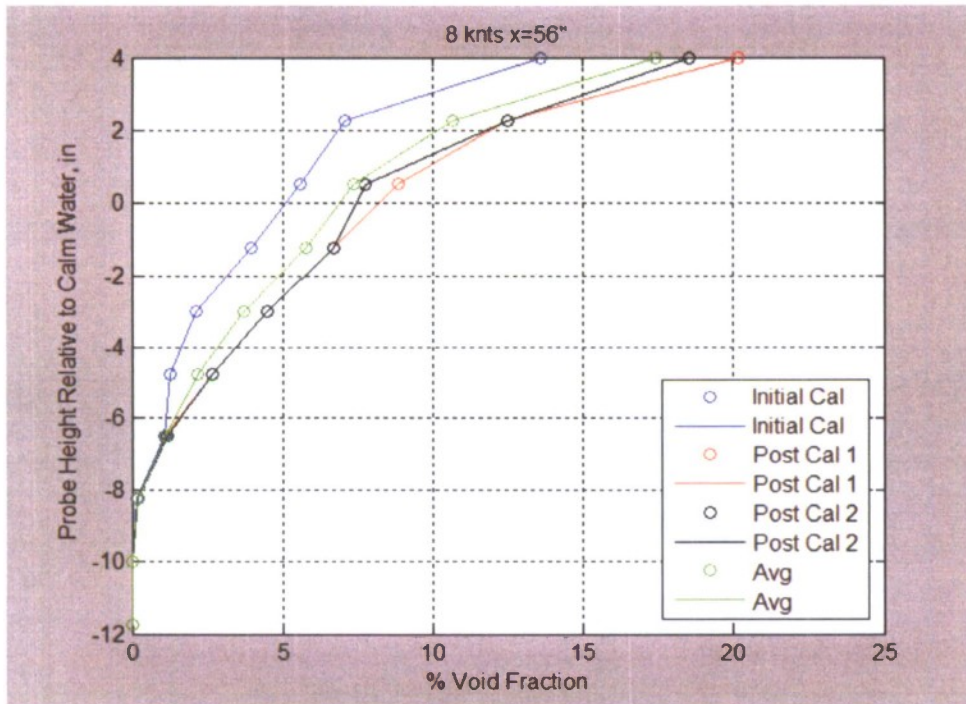


Figure A-5. Probe Height vs. Void Fraction at 8 knots for longitudinal location x=56".

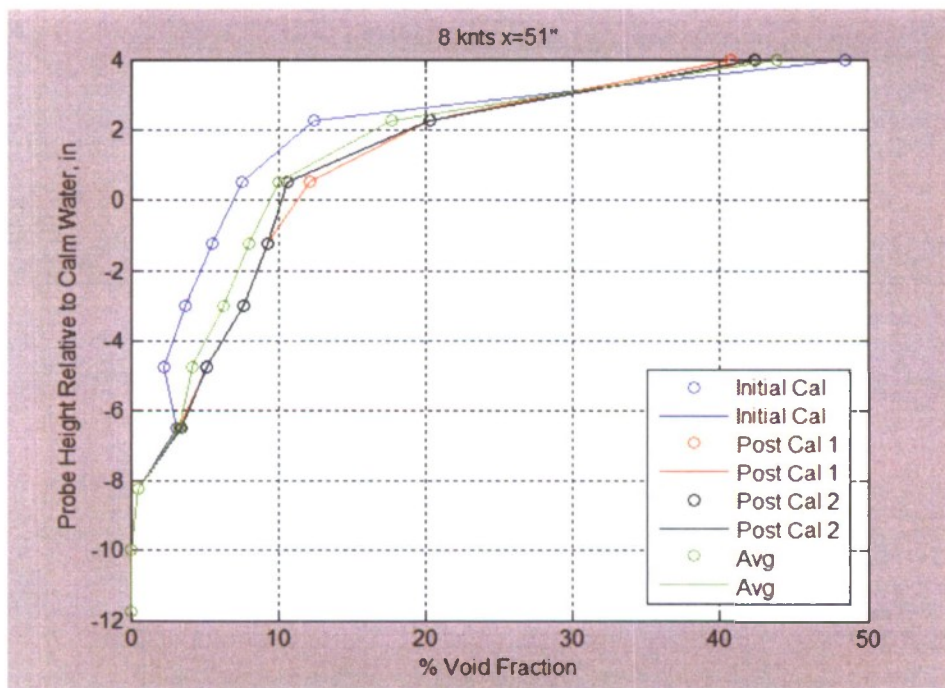


Figure A-6. Probe Height vs. Void Fraction at 8 knots for longitudinal location x=51".

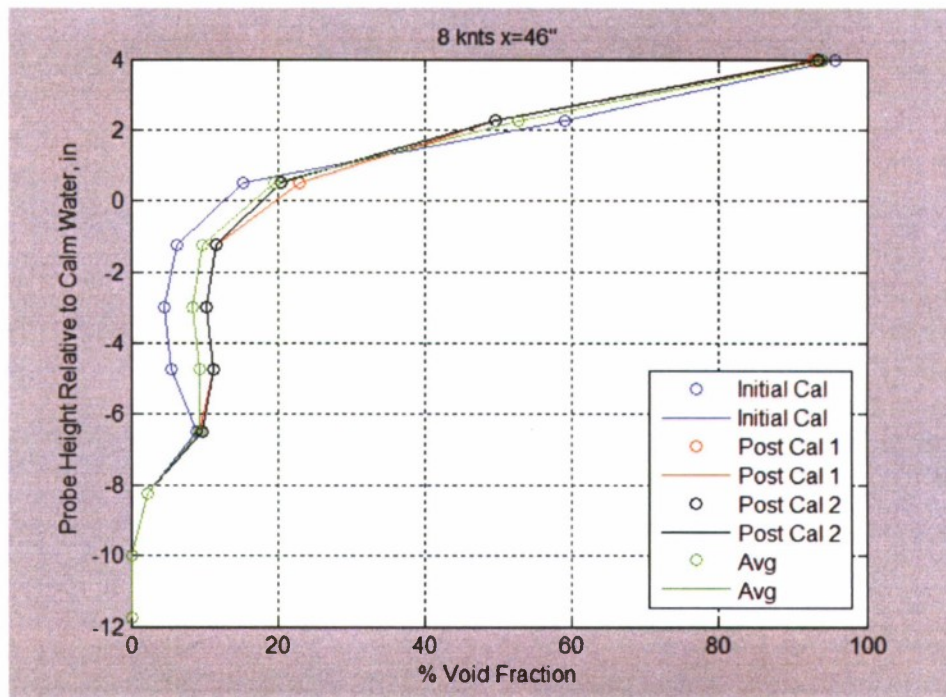


Figure A-7. Probe Height vs. Void Fraction at 8 knots for longitudinal location $x=46''$.

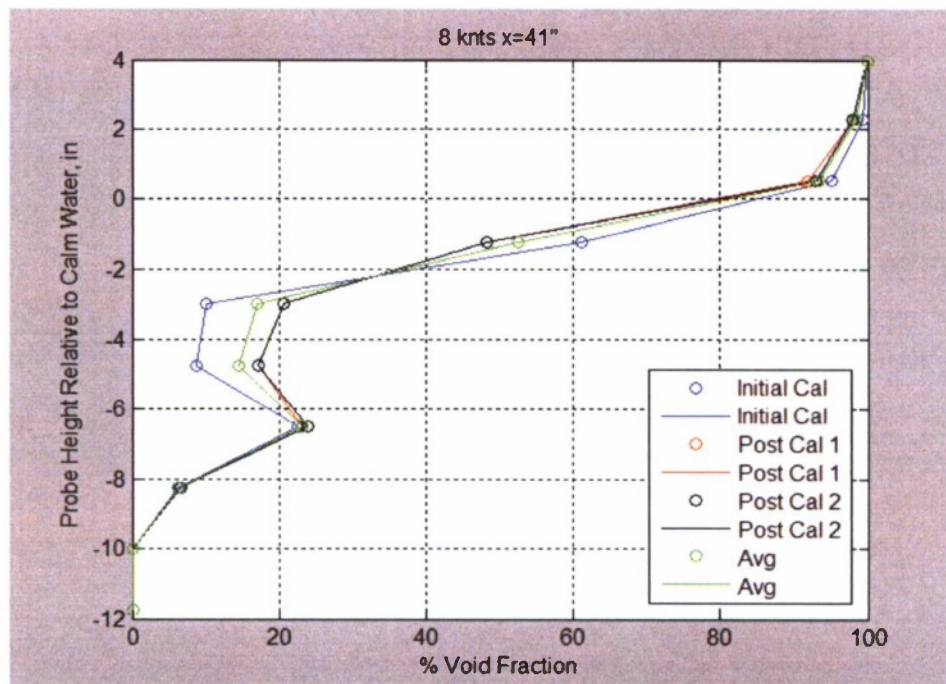


Figure A-8. Probe Height vs. Void Fraction at 8 knots for longitudinal location $x=41''$.

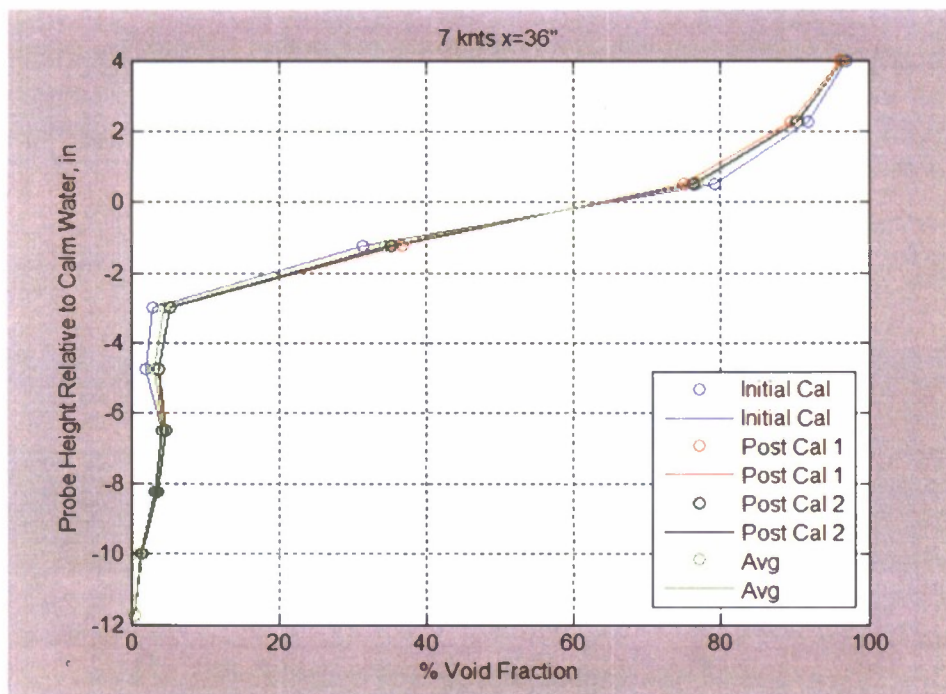


Figure A-9. Probe Height vs. Void Fraction at 7 knots for longitudinal location $x=36''$.

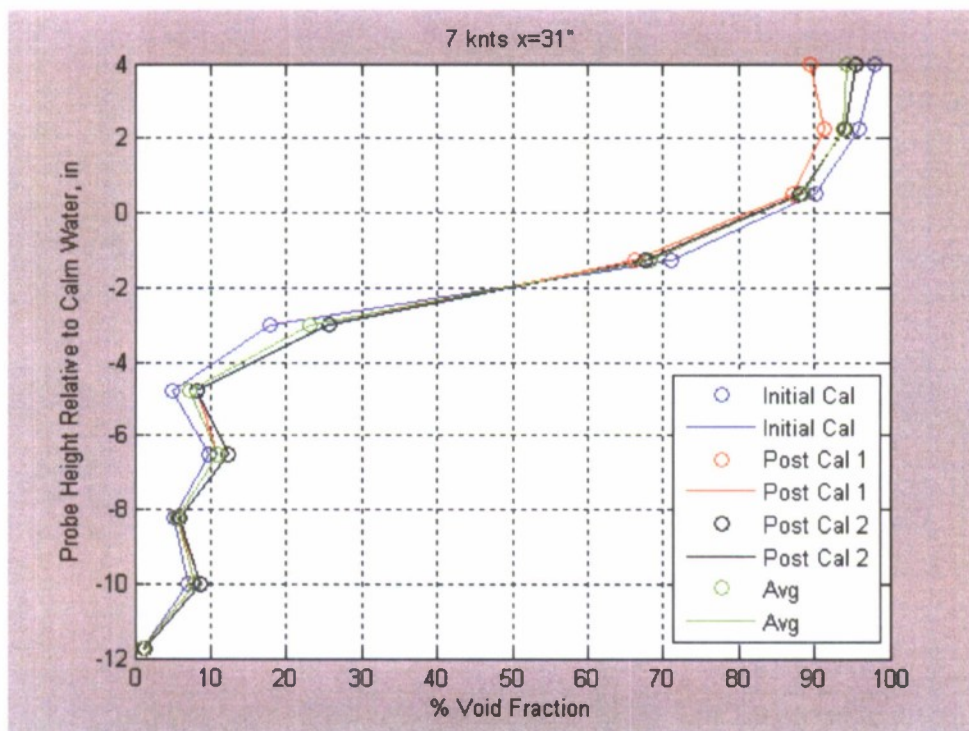


Figure A-10. Probe Height vs. Void Fraction at 7 knots for longitudinal location $x=31''$.

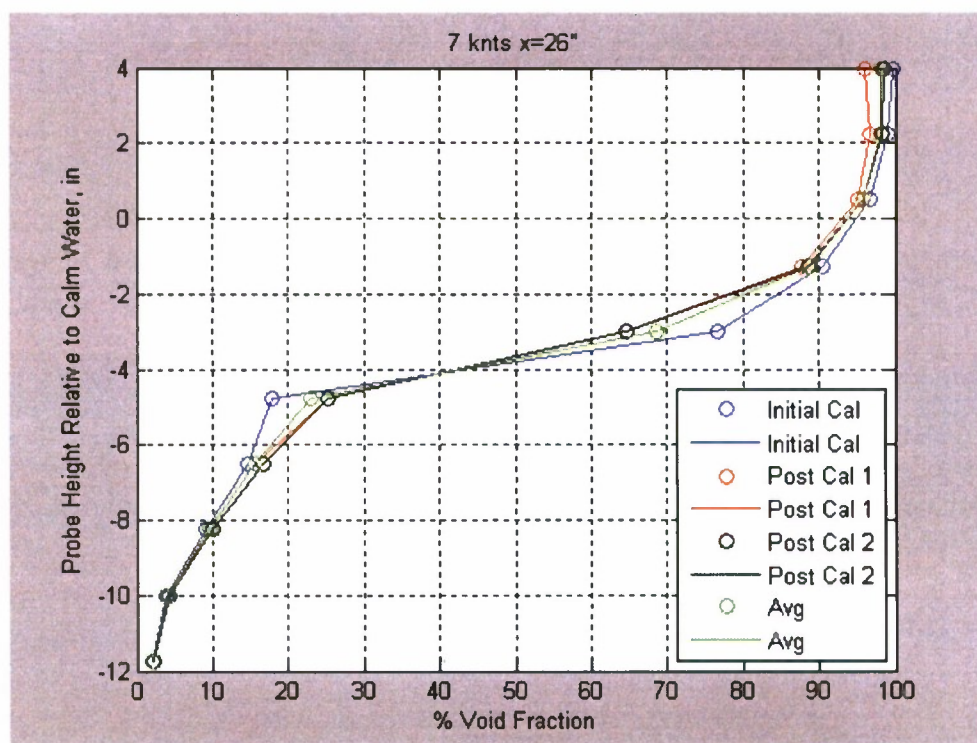


Figure A-11. Probe Height vs. Void Fraction at 7 knots for longitudinal location $x=26''$.

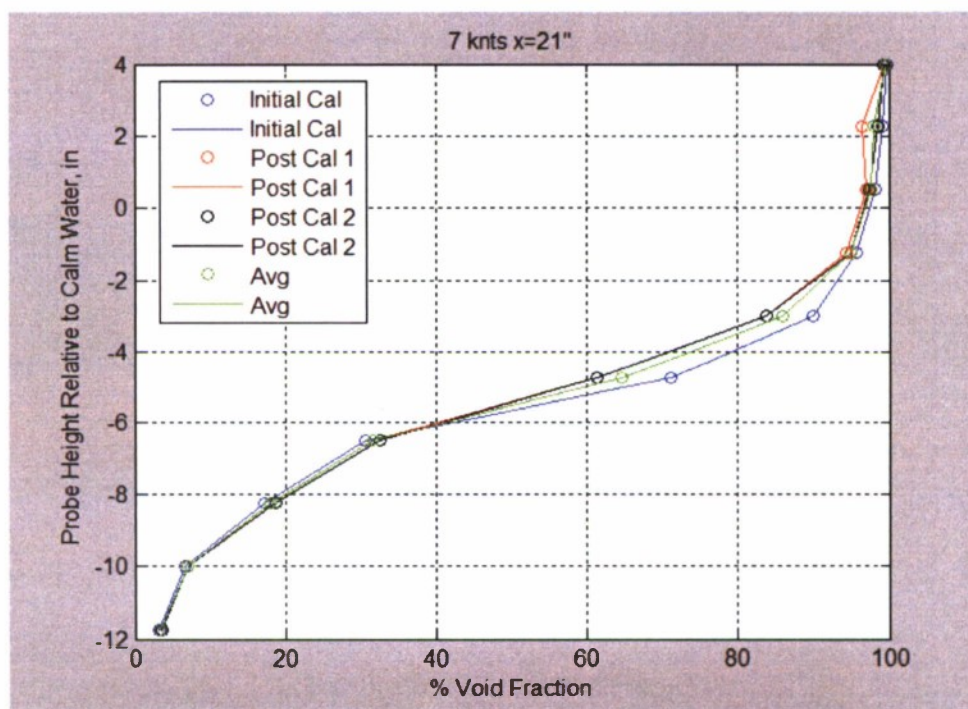


Figure A-12. Probe Height vs. Void Fraction at 7 knots for longitudinal location $x=21''$.

REFERENCES

1. Saunders, H. E. "The David W. Taylor Model Basin, Parts 1, 2 & 3," SNAME Transactions Volumes 46, 48 & 49, 1938, 40 & 41.
2. Maki, K. J., Doctors, L. J. and R. F. Beck. "On the Profile of the Flow Behind a Transom Stern." *Ninth International Conference on Numerical Ship Hydrodynamics*, Ann Arbor, MI, 2007.
3. Faltinsen, O. *Hydrodynamics of High-Speed Marine Vehicles*. Cambridge University Press, New York, 2005.
4. Furey, D.A., and Fu, T.C. "Quantitative Visualization (QViz) Hydrodynamic Measurement Technique of Multiphase Unsteady Surfaces," *Proceedings of the 24th Symposium on Naval Hydrodynamics*, Office of Naval Research, 2002.
5. Rice, J.R., Walker, D.C., Fu, T.C., Karion, A. and T. Ratcliffe. "Quantitative Characterization of the Free-Surface Around Surface Ships," *Proceedings of the 25th Symposium on Naval Hydrodynamics*, Office of Naval Research, 2004.
6. Waniewski, T.A. "Air Entrainment by Bow Waves," Ph.D Thesis, California Institute of Technology, Pasadena, CA, 1999.
7. Coakley, D.B., Haldeman, P.M., Morgan, D. G., Nicolas, K.R., Penndorf, D.R., Wetzell, L. B., and Weller, C. S. "Electromagnetic Scattering From Large Steady Breaking Waves," *Experiments in Fluids*, 30, 479-487, 2007.
8. Fu, T.C., Fullerton, A.M., Terrill, E., and Lada, G., "Measurements of the Wave Field Around the R/V Athena I," *Proceedings of the 26th Symposium On Naval Hydrodynamics*, Rome, Italy, 2006.
9. Fu, T.C., Rice, J.R., Terrill, E., Walker, D.C., and Lada, G., "Measurement and Characterization of Full-Scale Ship Waves," *Ships and Ship Systems (S3) Tech. Symposium*, Carderock, MD, 2006.
10. *Principles of Naval Architecture: Volume II-Resistance, Propulsion and Vibration*. Society of Naval Architects and Marine Engineers, Jersey City, New Jersey, 1988.

This page intentionally left blank.

DISTRIBUTION LIST

Copies		Name
3	SAIC	Chevalier, Dommermuth, Wyatt (pdf only)
2	CalTech	Gharib, Jeon (pdf only)
2	Iowa	Stern, Carrica (pdf only)
NAVSEA		
1	DTIC	
ONR		
1	331	Purtell
Division Distribution		
1	3452	Library (pdf only)
1	5060	Walden
5	5600	Anderson, Drazen, Minnick, Ratcliffe, Russell (pdf only)
2	5700	Brewton, Gorski (pdf only)
4	5800	Fu, Fullerton, Walker (pdf only), Files (2)